universität wien

# MASTERARBEIT

Titel der Masterarbeit

„Coherence strain effects in alkali feldspar“

Verfasserin

Katharina Sarah Scheidl B.Sc.

angestrebter akademischer Grad

Master of Science (M.Sc.)

Wien, 2012

| | |
|---|---|
| Studienkennzahl lt. Studienblatt: | A 066 815 |
| Studienrichtung lt. Studienblatt: | Erdwissenschaften UG 2002 |
| Betreuer: | Univ. Prof. Mag. Dr. Rainer Abart |

**Erklärung zum eigenständigen Verfassen der Arbeit**

Ich versichere, dass ich die vorliegende Arbeit selbständig verfasst und keine anderen als die angegebenen Quellen und Hilfsmittel verwendet habe. Die Arbeit wurde in gleicher oder ähnlicher Form noch nicht in einem anderen Studiengang als Prüfungsleistung verwendet.

Wien, am

Unterschrift

(Katharina Sarah Scheidl)

# Outline

## 1. Introduction

With 50 vol.-% the mineral group of the feldspars is the most abundant mineral group in the Earth´s upper crust. Feldspars can be found in almost all acidic, alkaline, intermediate or basic volcanic or plutonic rocks and also occur in many metamorphic rocks and frequently even in sediments. The compositions of nearly all natural feldspars are represented in the ternary feldspar diagram, shown in Figure 1, which is defined by the components orthoclase ($KAlSi_3O_8$), albite ($NaAlSi_3O_8$) and anorthite ($CaAl_2Si_2O_8$). Feldspars with compositions ranging between albite and anorthite are defined as plagioclase feldspars while those ranging between albite and orthoclase are classified as alkali feldspars. The alkali feldspars exhibit a complete solid solution at high temperatures and show a miscibility gap below about 650 °C (see Figure 1).The end members anorthite and orthoclase appear to be immiscible. Very uncommon in natural samples is the barium-rich feldspar $BaAl_2Si_2O_8$ referred to as celsian, but it is still found as a component in potassium-rich feldspars.

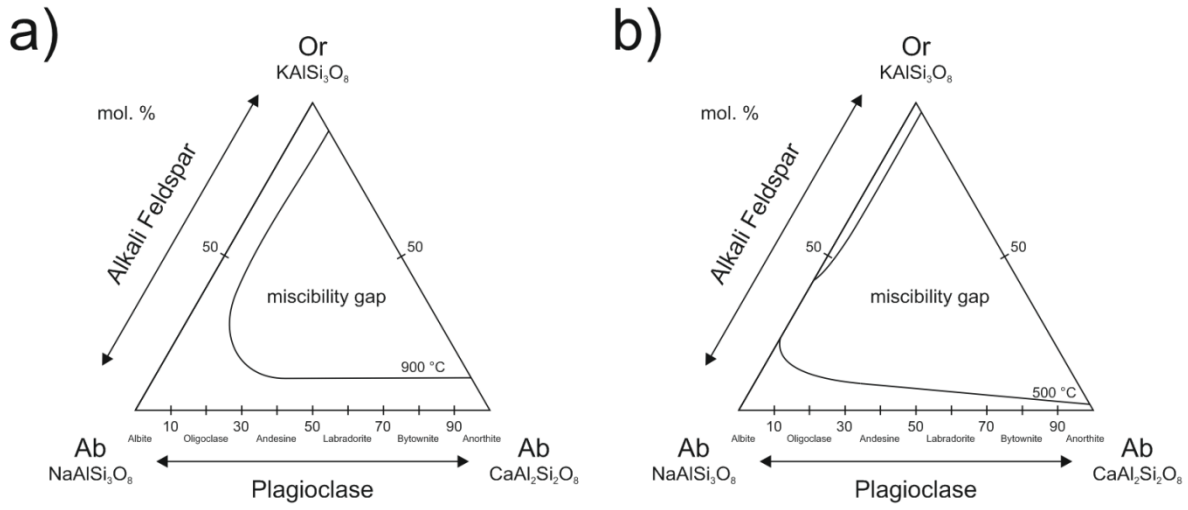


**Figure 1: The ternary feldspar diagram An-Ab-Or for a) 900 °C and b) 500 °C; there exists a solid solution between the alkali feldspars for high temperatures, but with decreasing temperatures the miscibility gap in the ternary system and thus in the binary system of the alkali feldspar broadens; image modified after Okrusch and Matthes (2009)**

When alkali feldspars are subject to cooling and heating processes or composition changes they undergo a variety of phase transformations and structural changes; these include monoclinic-triclinic transformation, (Al, Si) ordering on the tetrahedra sites, twinning and exsolution. These processes depend on the formation conditions and cooling history of the

feldspars. For this reason many experiments in the laboratory imitating the processes of nature have been done to understand their underlying parameters. These studies provide an understanding of thermodynamic processes such as element partitioning between feldspar and a fluid and a vapor phase, respectively, (Orville 1963; Sipling and Yund, 1976; Neusser et al., 2012) as well as kinetic processes such as microstructure evolution (Yund and Davidson, 1978; Parsons et al., 2010; Norberg et al., 2011). The conclusions of those experiments are then transferred to natural samples which bear important information for reconstructing the origin and development on the basis of their microtextures. Associated with geochronology such as $^{40}K/^{40}Ar$ dating for potassium-rich feldspars a model of the geological history of crustal rocks is feasible.

During changes in temperature and composition alkali feldspars exhibit different microstructures. Flude et al. (2012) distinguish two types of microtextures according to their formation mechanism. The first are the strain-free microtextures formed by dissolution-reprecipitation reactions as a consequence of hydrothermal or deuteric fluid interactions with the alkali feldspar. Pluemper and Putnis (2009) describe how the characteristics of reprecipitated feldspar phases can be used to understand the evolution of hydrothermally alterated granitoid rocks. The second types are the microtextures formed by exsolution and ordering processes such as perthitic lamellae and twinning. Their orientations are determined by the anisotropic interfacial strain energy. Note that these are formed by change of temperature, and so can provide information about the cooling history of the rocks (Abart et al., 2009; Yuguchi and Nishiyama, 2007; Brown et al., 1983).

This work deals with the mechanisms underlying the second type of microstructures. The exsolution of alkali feldspar single crystals leads to the formation of cryptoperthites; that means perthites with exsolution lamellae on the nm scale and thus not even visible under the optical microscope. Cryptoperthites are composed of sodium- and potassium-rich domains while the tetrahedra network remains intact. The lattice parameters differ in these two domains and therefore the lattices of both phases must resize. As a consequence elastic strain develops and the two phases arrange themselves in such a manner that minimizes the strain.

In the course of the following work, two sanidine feldspars are reacted with sodium-rich salt melt. Thus a misfitting surface layer develops, where the lattice parameters have to adapt to the volumetrically dominant core. For small composition shifts this adjustment is elastic, but as soon as a critical value of composition shift is exceeded brittle fracturing occurs. For shifts of potassium-rich to sodium-rich feldspars a regular crack pattern parallel to a general crystallographic plane develops. This process is already described in Neusser et al. (2012). There the orientation of the cracks is characterized in detail and a mechanical stress analysis for chemical-induced fracturing on the (010) plane of alkali feldspar is presented. The aim of this work is to give more precise values for the determination of the critical strain and thus of the critical stress, and to perform a detailed derivation for the mechanical stress analyses.

The actual outline of the experiment is preceded by an introduction to the structure of the feldspar with emphasis on structural changes and exsolution in chapter 2. In the next step, the characteristic processes of exsolution and diffusion are presented as the key triggers for feldspar fracturing. The following chapters 3 and 4 describe the experimental setup as well as the analytical methods. Chapter 5 then illustrates the main findings of the experiments while the next part of the theses features a discussion of the driving forces and mechanics involved in the fracturing processes. As the last point of this thesis, chapter 7 is dedicated to the evaluation of the conclusions drawn so far. The reason for formation of cracks with a regular orientation is pointed out and the strain analysis is performed.

## 2. Alkali feldspar

Since the crystal structure of feldspar is a basic aspect for the understanding of the diffusion mechanism in feldspar, this introductory chapter will first give a brief overview of the structure of the sample material. Drawing on these explanations, the following paragraph will then illustrate diffusion and exsolution which are the underlying processes for the formation of cracks.

### 2.1 Structure of feldspar

The crystal structure of feldspar is uniquely characterized by its tetrahedral framework. In the following the structure is described in general with regard to the exsolution process and

structural changes. Since it is not relevant to the subject of this work, the ordering process of Al and Si on the tetrahedra sites will not be adressed. For further details refer to Ribbe (1986) and Deer at al. (2001).

Feldspar minerals belong to the group of framework silicates. Their $(AlSi_3O_8)^-$ network is formed by corner-shared (Al, Si) tetrahedra, whose large and irregular cavities are filled with cations - in alkali feldspar the monovalent $K^+$ and $Na^+$ - for charge balance, depicted in Figure 2. Feldspar crystallizes in a monoclinic C2/m or a triclinic $C\bar{1}$ crystal structure depending on the chemical composition and the temperature of crystallization.

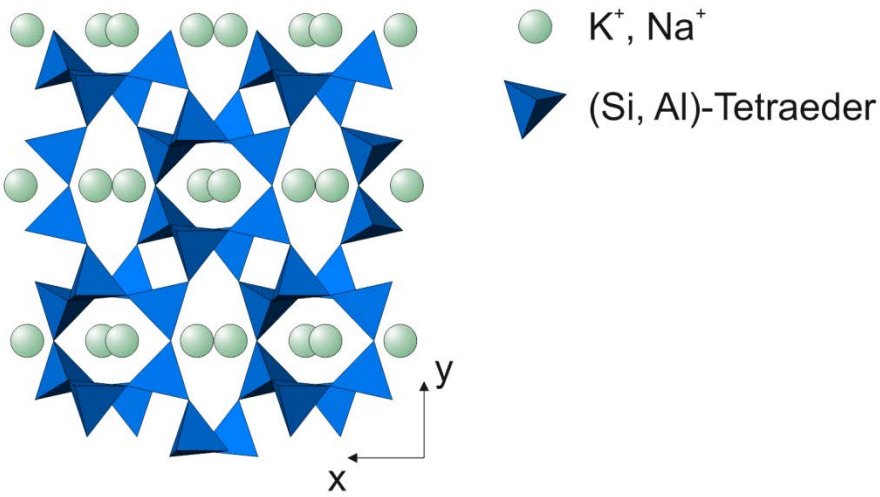


**Figure 2: Schematic drawing of the sanidine (Al, Si) network with view onto (001); the three dimensional network with the cations in the large, irregular cavities is visible; low sanidine data from Phillips and Ribbe (1973); created with Atoms**

The key units of the network are rings of four corner-shared (Al, Si) tetrahedra, illustrated in Figure 3. The tetrahedra rings are again corner-shared and form crankshaft-like chains parallel to the a-axis (see Figure 4). The crankshaft chains consist thus of two kinds of tetrahedral rings: rings arranged perpendicular to the b-axis and rings stacked in an alternating tilted manner along the a-axis.

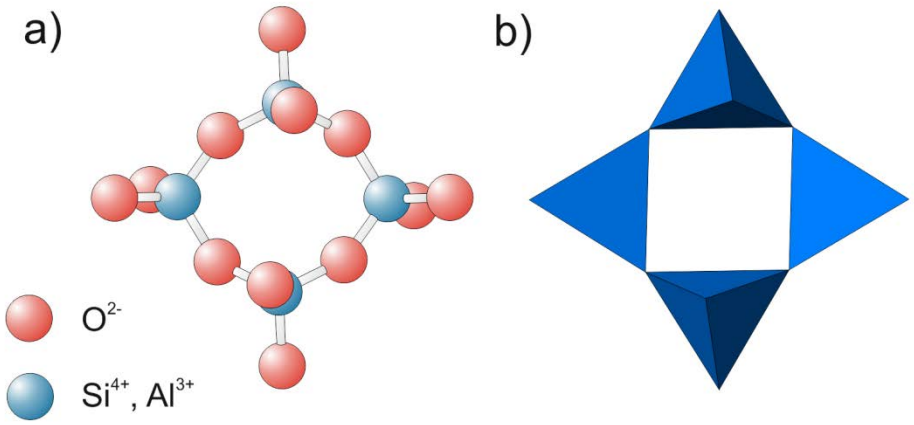


**Figure 3: Four-membered rings of (Al, Si) tetrahedra as key units of the tetrahedral network; low sanidine data from Phillips and Ribbe (1973); created with Atoms**

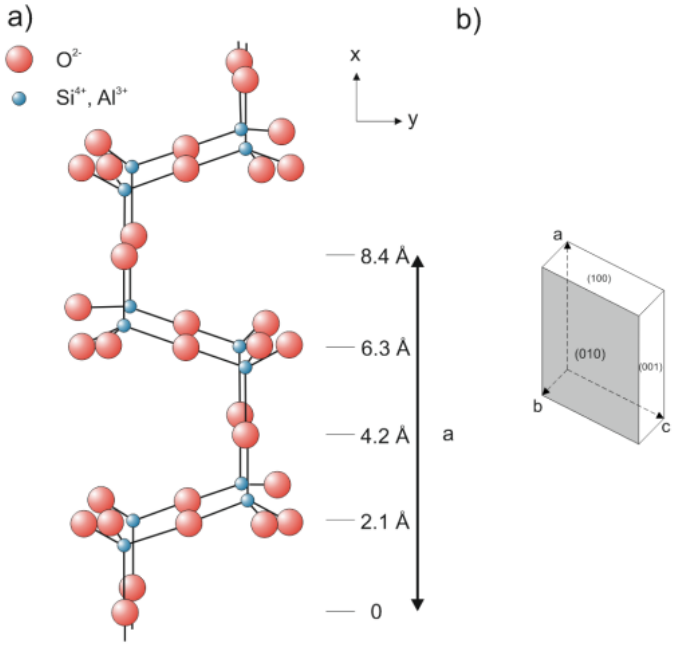


**Figure 4: Crankshaft-like chains built up of four-membered tetrahedral rings running parallel along the a-axis; low sanidine data from Phillips and Ribbe (1973); created with Atoms**

On the $(20\bar{1})$ plane, this results in a projection on a plane of the tilted rings which are approximately normal to the a-axis, the rings are further corner-shared and form a layer of corner-shared tetrahedra rings (Figure 5).

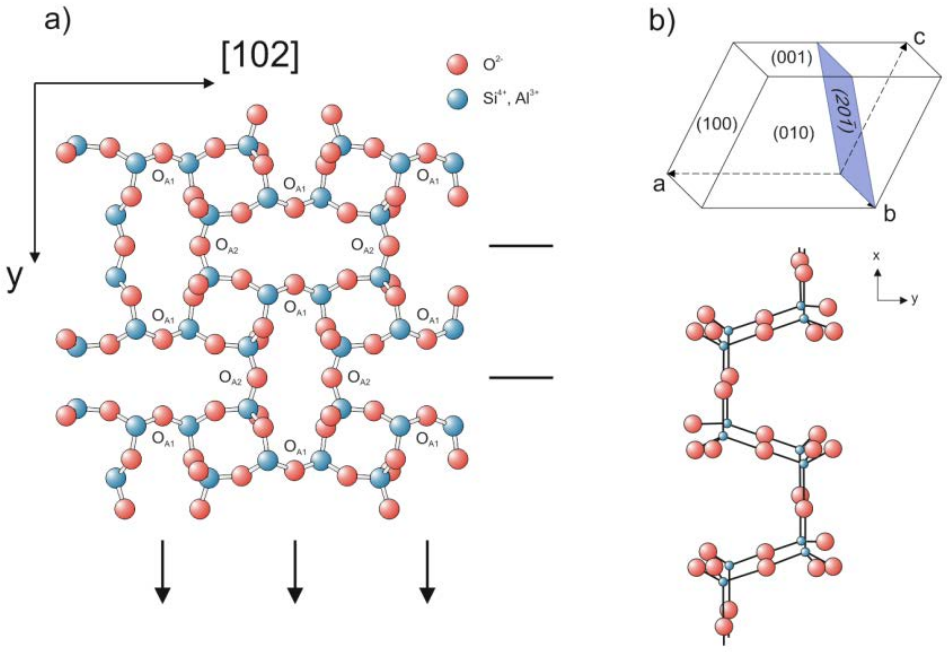


**Figure 5: Projection onto the (20$\bar{1}$) plane; low sanidine data from Phillips and Ribbe (1973); created with Atoms**
**a) Projection onto the (20$\bar{1}$) plane illustrating the sheet of corner-shared tetrahedral rings**
**b) Scheme of the (20$\bar{1}$) plane**

The crankshaft chains are again corner-shared parallel to the b- and c-axis and form layers of crankshaft chains parallel to the (001) and the (010) plane, respectively (Figure 6 and Figure 7).

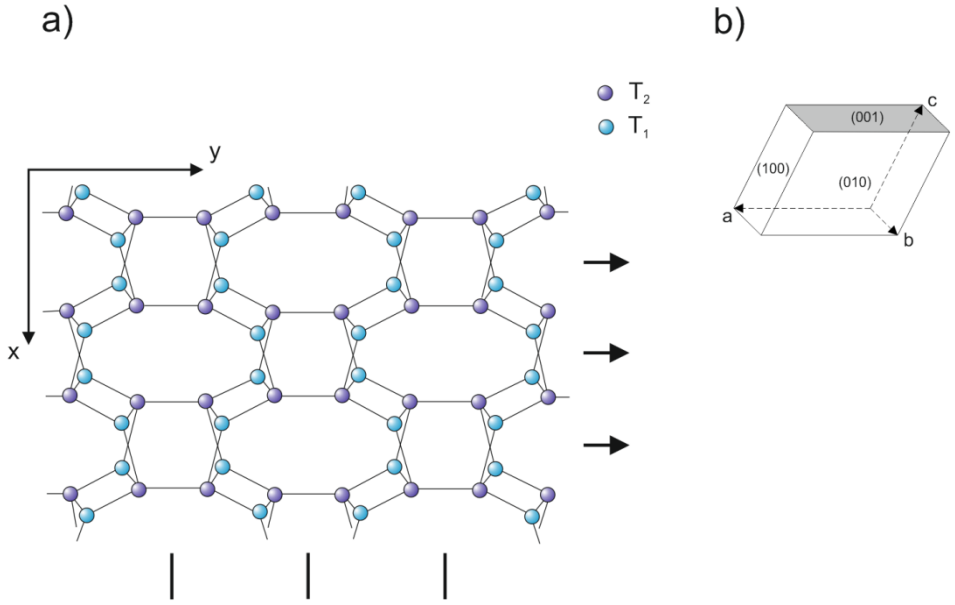


**Figure 6: View on the (001) plane; depicting the connections of the crankshaft-like chains along the b-axis; image modified after Ribbe (1986)**

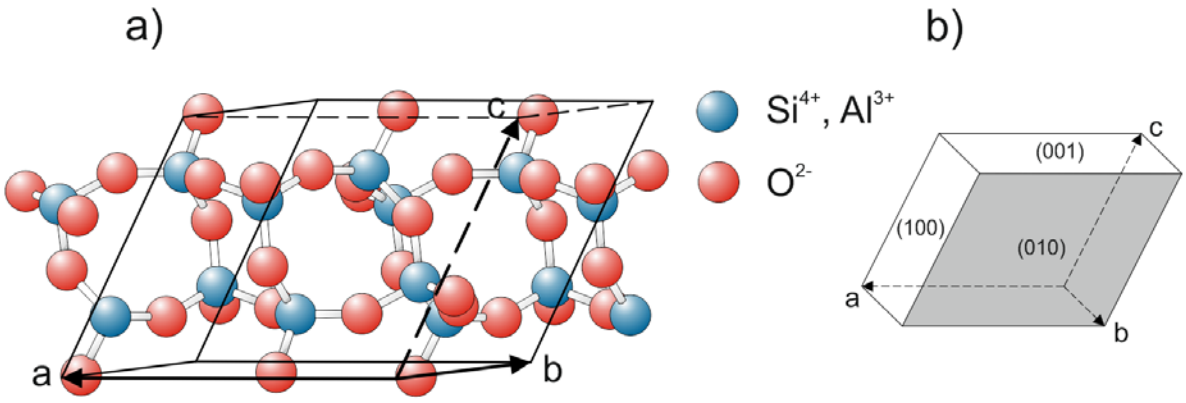


**Figure 7: Projection on the (010) plane showing the bindings of the crankshaft-like chains along the c-axis; low sanidine data from Phillips and Ribbe (1973); created with Atoms**

On the basis of these connected crankshaft chains over shared oxygen atoms parallel to the b- and c-axis it is possible to explain the perfect (010) and (001) cleavage planes.

The two cations $K^+$ and $Na^+$ differ obviously in their ionic radii of 1.59 Å and 1.25 Å, respectively (Okrusch and Matthes, 2009), illustrated in Figure 8a. In potassium-rich feldspar the larger $K^+$ atom is able to hold a monoclinic tetrahedra network; around the smaller $Na^+$ the network collapses and thus forms a triclinic lattice (Figure 8b). At higher temperatures the effective radius of the $Na^+$ is enlarged by thermal vibration and the lattice of the triclinic network converts to a monoclinic system. This process is reflected in the transformation of monalbite to analbite. The different ionic radii also account for the exsolution process; the lattice axis for the alkali feldspars increases with increasing mole fraction $X_{Or}$ ($X_{Or} = \frac{n_K}{n_K + n_{Na}}$). The capacity for incorporating the larger $K^+$ in sodium-rich alkali feldspar thus decreases with decreasing temperature and vice versa; thus the miscibility gap broadens with decreasing temperature. This will be illustrated by thermodynamic considerations in the next paragraph.

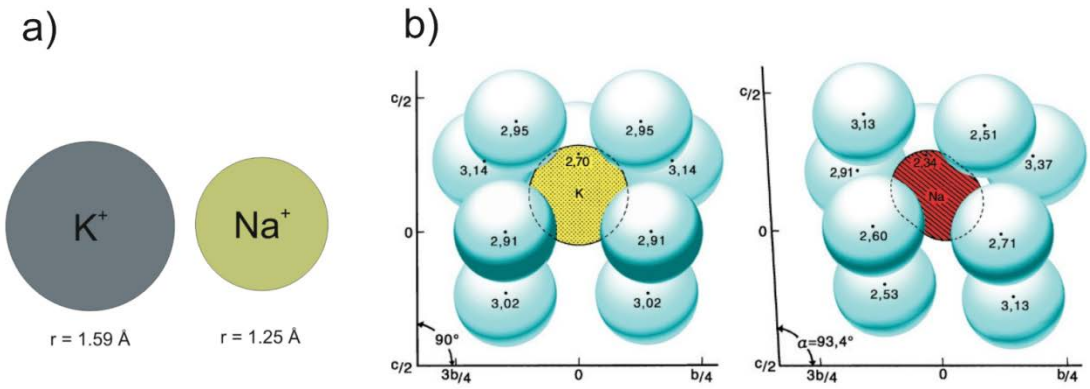


**Figure 8: Influence of the cation radii on the lattice structure;**
**a) Relative proportions of the cations; data from Okrusch and Matthes (2009)**
**b) Projection onto the (100) plane; oxygen atoms coordinating $K^+$ (on the left site) in C2/m high sanidine and $Na^+$ in CI analbite (on the right site); collapse of the lattice around the smaller $Na^+$; the distances between the cation and the oxygen atoms are given in Å; image taken from Okrusch and Matthes (2009)**

In contrast to the (Al, Si) tetrahedra the $K^+$ is coordinated by nine and the $Na^+$ by six to seven oxygen atoms and thus the bond strengths are rather weak for the cations. For this reason the cations are mobile during diffusion processes while the (Al, Si) tetrahedra network does not change.

## 2.2 Exsolution

Figure 9a displays the binary phase diagram of alkali feldspars. At higher temperatures they form a solid solution series with complete miscibility but at lower temperatures, depending on the composition, exsolution occurs. A mismatch between the potassium-rich and the sodium-rich phase is caused by the different lattice dimensions at a given temperature. While an alkali feldspar of intermediate composition is cooled from high temperature below the solvus segregation into two phases is initiated. The resulting intergrowths are called crypto- micro- or macropethite, depending on the width of the lamellae. In cryptoperthites the phase separation only takes place on the cation sites whereas the tetrahedral network remains intact. Exsolution is driven by the fact that the homogeneous phase becomes thermodynamically unstable or metastable, i.e. energetically less favorable than a mechanical mixture of the separated phases. Exsolution may occur by two different processes, namely by spinodal decomposition or by nucleation and growth (Huston et al.,

1966). These mechanisms are followed by coarsening, which is controlled by interdiffusion of $Na^+$ and $K^+$ (Abart et al., 2009).

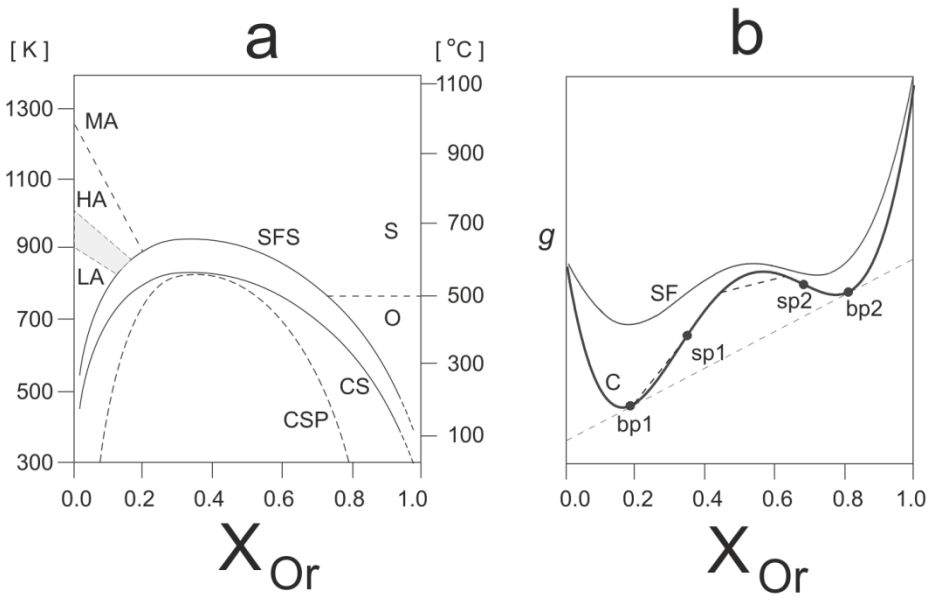


**Figure 9:**
**a) Solvus curves for alkali feldspars (CS) and strain-free solvus (SFS); S: sanidine, O: orthoclase, MA: monalbite, HA: high albite, LA: low albite; image modified after Brown and Parsons (1984)**
**b) g-X diagram for alkali feldspars at a certain temperature; image taken from Abart et al. (2009)**

In Figure 9a two different kinds of solvi are shown, the strain-free solvus (SFS) and the coherent solvus (CS). In Abart et al. (2009) it is explained how these two solvi are defined. Equilibrium between two exchanged phases is reached when the value for the Gibbs free energy is minimized. During slow cooling of an alkali feldspar the two coexisting phases constantly readjust their equilibrium compositions. The g-X diagram in Figure 9b illustrates the paragenesis of two alkali feldspar phases with minimized Gibbs free energy for a given temperature. For a single crystal of alkali feldspar only the cations separate during an interdiffusion process into two domains with different composition. This process is termed spinodal decomposition when it starts within the spinodal region, shown in the g-x diagram (Figure 9b). Otherwise the exsolution would start within the metastable region of the phase diagram; this mechanism is termed nucleation and growth. Because of the different lattice dimensions of the two phases the lattices of the two domains do not match and thus the coherent (Al, Si) tetrahedral framework is strained. This coherency strain is expressed in an

energy function that counteracts the Gibbs free energy and in turn the exsolution process. Hence, the temperature for phase separation is lower for feldspar with a coherent tetrahedra network (coherent solvus) than for strain-free exsolved grains (strain-free solvus). The orientation of the lamellae in cryptoperthites can be explained on the basis of the coherence strain. The interface between the two differently composed domains is arranged in a manner that minimizes the coherence strain energy. The preferred faces are observed as the ($\bar{8}$01) and ($\bar{6}$01) for intergrown monoclinic phases (Bollmann and Nissen, 1968).

## 2.3 Diffusion

Diffusion is important for many mineralogical processes and reactions such as element partitioning between solids or between solids and fluids, ordering and exsolution. The diffusion coefficient of the respective elements determine to what extent element partitioning or chemical zoning is preserved during cooling over geologically relevant time scales. For alkali feldspars the diffusion of the cations $K^+$ and $Na^+$ plays a role for exsolution as already described in the chapter on exsolution.

For the experiments discussed in this work sanidine feldspar was exchanged with a NaCl – KCl-salt melt in order to shift the initial orthoclase-rich composition to more albitic-rich compositions. The exchange of $K^+$ and $Na^+$ between the salt melt and the feldspar is facilitated by a diffusion process. Another possibility that accounts for the replacement of an orthoclase-rich feldspar with a more albite-rich phase might be found in the dissolution-reprecipitation process, described in Putnis (2002) and Norberg et al. (2011). In comparison to the products of the new sodium rich feldspar developed in the process of dissolution-reprecipitation the exchanged domains presented in this work show several differences. In contrast to the dissolution-reprecipitation samples the reaction front in the samples in this work is smooth and extends over several µm to several tens of µm. In addition the concentration of Ba remains constant over the transition between the exchanged and original domains. This finding is demonstrated in microprobe analysis. In products of dissolution-reprecipitation the concentration of minor and trace elements differs in the newly grown zone. Furthermore, the (Al, Si) distribution is the same both in the exchanged and in the original feldspar. In a newly grown reprecipitated phase, however, the (Al, Si)

distribution would always be disordered. Finally, the new albitic phase displays no porosity unlike that observed in reprecipitated products. These criteria coincide with the assumption of a diffusion process in which the $K^+$ and $Na^+$ exchange takes place on the cation sublattice whereas the (Al, Si) tetrahedral network remains unmodified.

Diffusion is defined as the process of material transport which is driven by a gradient in concentration and therefore in the chemical potential. Diffusion is the relevant process for exsolution and homogenization under dry conditions, ordering and disordering of Al and Si on the tetrahedra sites. Furthermore, it facilitates cation exchange between feldspar and melt, fluid or any solid and hence plays a major role in the development of alkali feldspar microstructures. The flux of diffusing material is described by Fick's first law (Crank, 1975):

$$J = -D\frac{\partial c}{\partial x}$$

with J for the flux, D for the diffusion coefficient, x for the position and t for the time. The flux J is connected to the concentration gradient by the diffusion coefficient D. Fick's second law relates the change in concentration with time and position (Crank, 1975):

$$\frac{\partial c}{\partial t} = D\frac{\partial^2 c}{\partial x^2}$$

Diffusion in crystals is more complex because of their anisotropy. Furthermore, the diffusion coefficient is temperature and pressure dependent. The temperature dependence is given by Arrhenius' equation:

$$D = D_0 e^{-\frac{E}{RT}}$$

with D for a diffusion coefficient at a given temperature T and $D_0$ for the pre-exponential factor. E is the activation energy and R the gas constant.

Experiments to determine the diffusion coefficient for alkali feldspar were done by Christoffersen et al. (1983). Their findings imply that the $Na^+/K^+$ interdiffusion coefficient is dependent on the composition of the feldspar; it increases with rising mole fraction $X_{Or}$. Furthermore, diffusion perpendicular to (001) is much faster than perpendicular to (010) thus, the diffusion coefficient is highly anisotropic as shown in Figure 10.

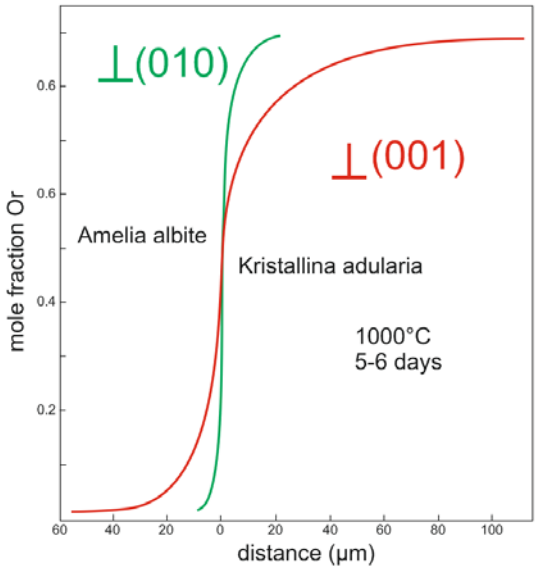


**Figure 10: Diffusion profiles for alkali interdiffusion, measured using an electron microprobe, show that the diffusion coefficient is higher perpendicular to (001) than perpendicular to (010); image modified after Christoffersen et al. (1983)**

## 3. Experimental

After a detailed description of the exsolution and diffusion processes, the following paragraph focuses on the exchange experiment and the associated fracturing. In the first section there will be an introduction to the starting material after which the sequence of the Na  K exchange experiment is outlined.

### 3.1 Starting material

As starting martial for the experiments, gem-quality sanidine feldspars from two different localities in the Eifel were used. The sanidine from Volkesfeld is composed of $Or_{84}Ab_{15}Cs_{01}$ whereas that of the sanidine from the Rockeskyller Kopf is composed of $Or_{72}Ab_{26}Cs_{02}$. The chemical analyses of both feldspars are given in Table 1. The two sanidines are characterized as monoclinic with the space group C2/m, have disordered (Al, Si) distribution and are homogenous on the nanometer scale (Neusser et al., 2012; Demtroeder, 2011). The crystals are optically clear and exhibit, apart from the (010) and (001) cleavage planes, no cracks. The crystals were crushed and sieved to a size of 100 – 200 µm. Further, cubes of 3 mm x 3 mm x 1 mm with polished (001) and (010) faces were prepared.

**Table 1: Chemical analysis of the starting materials**

| Phase | $SiO_2$ | $Al_2O_3$ | FeO | BaO | $Na_2O$ | $K_2O$ | MgO | Tot. | $X_{Or}$ | $X_{Ab}$ | $X_{Cs}$ |
|---|---|---|---|---|---|---|---|---|---|---|---|
| PR | 63.98 | 19.046 | 0.159 | 0.884 | 1.836 | 13.605 | 0.000 | 99.51 | 0.84 | 0.15 | 0.01 |
| EPR | 64.084 | 18.974 | 0.148 | 1.313 | 2.809 | 12.097 | 0.011 | 99.437 | 0.72 | 0.26 | 0.02 |

*PR: Volkesfeld sanidine, EPR: Rockeskyller Kopf sanidine*

## 3.2 Na – K exchange experiments

In the following Na – K exchange experiments about 0.1 g of crushed feldspar or one feldspar cube were reacted with NaCl – KCl salt melt in quartz glass tubes. The $X_{KCl}$ of the salt melt was varied based on the Na/K fractionation data for feldspar – salt melt equilibrium which is shown in Figure 11, in order to shift the feldspar to more albite rich compositions. To ensure a constant composition of the salt melt during the exchange experiments, the amount of the moles of cations in the salt exceeded the amount of the moles of cations in the feldspar by 40 times. In the next step the tubes were sealed under vacuum to guarantee that the exchange would take place under anhydrous conditions. The tubes were then annealed under ambient pressure at 850 °C in a muffle furnace for 7 to 32 days. The experimental setups are given in Table 2 and Table 3. After annealing the salt was dissolved with deionized $H_2O$ and the feldspar retrieved.

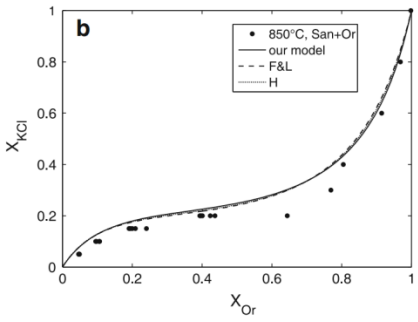


**Figure 11: Na/K fractionation data between salt melt and alkali feldspar; solid line: calculated Na/K partitioning curve based on Margules parameters obtained for 850 °C data; image taken from Neusser at al. (2012)**

The crushed feldspar samples were embedded in epoxy for analysis. The feldspar cubes were further prepared by cutting them perpendicular to the polished surfaces and embedding two differently oriented K- and L-plates in epoxy (see Figure 20).

## 4. Analytical techniques

### 4.1 Optical microscopy

The first observations were done with the help of optical microscopy. The fact that the cracks in the exchanged portions of the feldspar were already visible under the microscope turned out to be helpful for the further investigation of samples with very large crack spacing.

### 4.2 Scanning electron microscopy

For scanning electron microscopy and electron microprobe analyses the samples were coated with carbon.

For imaging of the cracks and the determination of the samples' orientation a Quanta 3D FEG and an Inspect S scanning electron microscope from FEI were used. SE and BSE images were taken at 10 to 15 kV beam acceleration voltage and an 8 nA beam current. The crystallographic orientations were identified with EBSD. For that the beam accelerating voltage was set to 20 kV and the beam current at 23 nA. The EBSD scans were done at 10 mm working distance and a tilt angle of 70° with 15 µm step size. For the recording, indexing and analyzing of the EBSD patterns the EDAX-TSL software OIM was used. The pole figures displayed in this work show the lower hemisphere and the faces (100), (010) and (001).

### 4.3 Electron microprobe

The chemical composition of the exchanged rim was analyzed with an electron microprobe (Cameca SX 100). The measured elements were Na, K, Fe, Ba, Mg, Al, Si, O. The acceleration voltage was set to 15 kV, the beam current to 20 nA. Orthoclase was used as standard. Due to the vulnerability of the feldspar the measurements were done with a 6 µm defocussed beam. Because of the small exchange rims of the samples with short run durations of 7 or 8 days, the beam spot was too broad to measure only the exchanged zones. In the 16 days samples the spacing of the cracks was too narrow to measure zones between the cracks. As a consequence, the results of the analyses were a mixture of the exchanged zones and the initial feldspar. The calculated $X_{Or}$ in these samples were systematically too high and

therefore not usable. Only in the samples with run duration of 32 days did the results coincide with the Na/K fractionation data for feldspar - salt melt equilibrium. For this reason all denoted $X_{Or}$ of the exchanged feldspars were taken from the fractionation diagram.

# 5. Results

## 5.1 Characteristics of the cracks

The following chapter outlines the findings about the cracks detected in the experiments.

The results suggest that the $X_{KCl}$ of the salt melt is responsible for the characteristics of the crack pattern. When the sanidine is shifted to a more orthoclase-rich composition ($X_{KCl} > 0.5$) a core-rim structure develops and eventually cracks form along the transition region between core and rim. When, however, the feldspar is shifted to a more albitic-rich composition a regular hierarchical pattern of cracks forms. Figure 12 shows these two kinds of crack patterns. This work deals with the hierarchical crack pattern since the regular fracturing allows a mechanical strain analysis. In a previous work by Neusser et al. (2012) the chemically induced fracturing in alkali feldspar and therefore the hierarchical crack pattern is already described. These observations correspond to the observations made in this work.

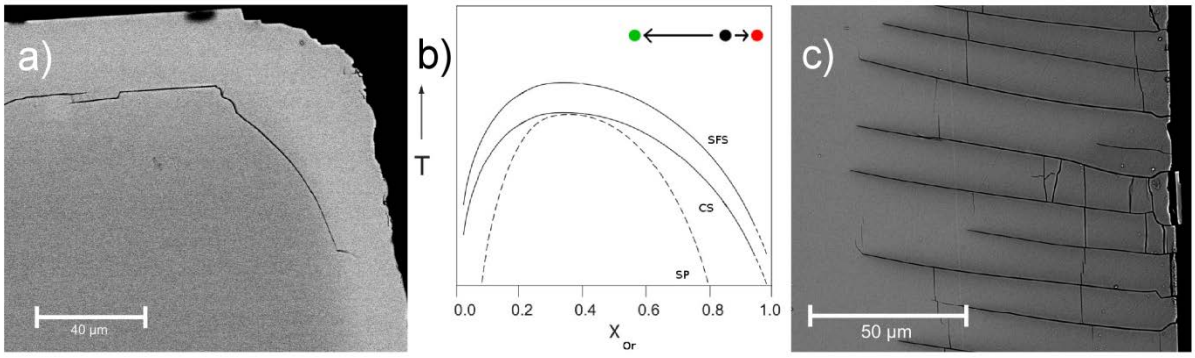


**Figure 12: Different crack patterns depending on the direction of the chemical shift**
**a) BSE image of Volkesfeld sanidine shifted to higher $X_{Or}$; exchanged $X_{Or}$ = 1.0; run durations: 16 days; image provided by courtesy of A.-K. Schaeffer**
**b) Schematic depiction of the shift in composition during the experiments; black: initial composition of PR; green: shift to lower $X_{Or}$; red: shift to higher $X_{Or}$**
**c) BSE image of Volkesfeld sanidine shifted to lower $X_{Or}$; exchanged $X_{Or}$ = 0.5; run durations: 8 days**

The crack pattern is composed of two hierarchical levels. The first consists of a set of subparallel cracks which extends parallel to an arbitrary crystallographic plane and does not

follow any cleavage plane. The cracks of the second hierarchical level run locally perpendicular to the dominant cracks parallel to the (010) cleavage plane. Both these hierarchical sets are shown in Figure 13.

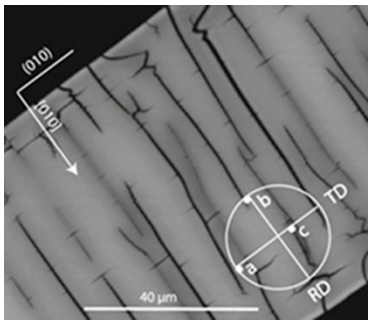


**Figure 13: First and second order cracks in Volkesfeld sanidine exchanged with salt NaCl-salt melt; the cracks of the first hierarchical order run parallel to the [010] direction; the traces of the second order cracks run perpendicular to b; image taken from Neusser et al. ( 2012)**

In the following paragraph, the characteristics of the first hierarchical set will be described in more detail. Figure 14 shows the orientation of the cracks. The dominant cracks extend parallel to a (h0l) plane and enclose an angle of 19-8° with the positive c-axis and an angle of 83°-72° to the positive a-axis measured from positive [100] to positive [001] (see Figure 15). In early stages of fracturing a few short cracks run perpendicular to the surface of the grains. With longer run durations the number of cracks increases and they become longer and extend parallel to a (h0l) plane. After a period of time no more crack development can be detected; at that point of the experiment crack spacing is between 5-40 µm depending on the composition of the original feldspar, of the salt melt and therefore on the chemical shift.

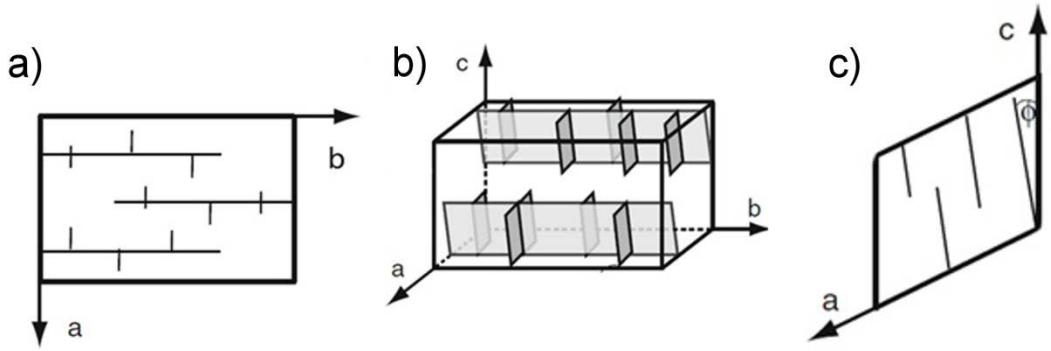


**Figure 14: Orientation of the cracks; image taken from Neusser et al. (2012)**
**a) View in the (010) plane that presents the angle Φ between the cracks and the c-axis**
**b) The orientation of the first and the secod hierarchical level cracks is illustrated.**
**c) A view onto the (100) plane is shown.**

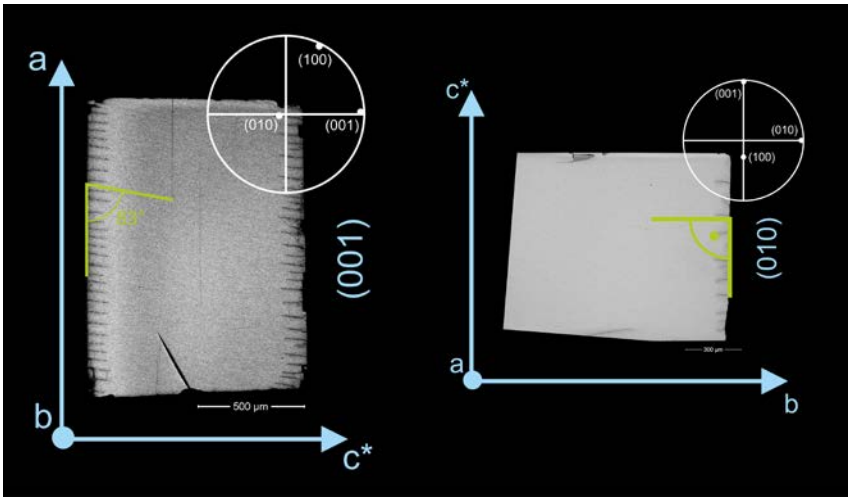


**Figure 15: Orientation of the cracks; image provided by courtesy of A.-K. Schaeffer**

When the feldspar is exchanged to very sodium-rich compositions, the cracks are bent in a saw tooth-shaped way, see Figure 22 (EPRb8_20). This effect is due to the fact that with the shift of the potassium rich sanidine to a sodium-rich analbite a monoclinic-triclinic transformation of the lattice takes place at approximately $X_{Or}$ = 0.4 (Kroll et al., 1986). As a consequence of this transition the triclinic albite-rich feldspar forms polysynthetic twins. Thus the twins lie perpendicular to the cracks and coincide with the saw tooth-shaped pattern.

During the process of the $Na^+/K^+$ exchange the composition continuously changes from the sodium-rich zones to the zones of the initial composition. At the same time the salt melt penetrates the cracks of the first hierarchical level. As a result the cracks form new surfaces where cation exchange takes place which leads to the formation of cracks of the second hierarchical level parallel to (010). This leads to exchange fronts progressing into the crystal both from the surface of the grain and from the cracks´ surfaces. With time the sodium rich zones get broader and neighboring zones overlap. This composition pattern is shown in Figure 16.

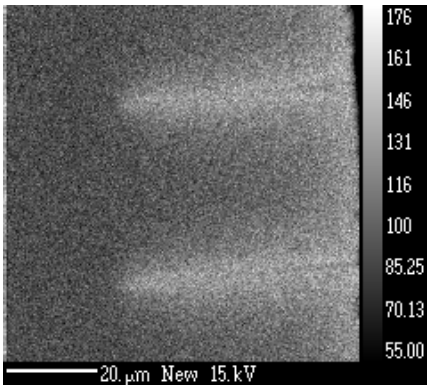


**Figure 16: A Na-map recorded with an electron microprobe is shown. It is illustrated how the sodium rich salt melt penetrates into the cracks of the first hierarchical level and therefore the diffusion on the new generated crack surfaces takes place; image provided by courtesy of A.-K. Schaeffer**

## 5.2 Critical shift for fracturing

As described before, the crack spacing depends on the chemical shift of the feldspar. The first experiments were mainly conducted to investigate the chemical shift required to initiate fracturing. In the first set of experiments crushed sanidine with initial $X_{Or}$ = 0.84 was used. The $X_{KCl}$ of the salt melt was varied in 0.01 mole steps and the run durations extended over a period of 7 days. The corresponding Na/K fractionation diagram between salt melt and the feldspar is shown in Figure 17. The results of the experiments are given in Table 2 and the BSE images of the treated samples are shown in Figure 18. As the results show, the first crack forms at $X_{Or}$ = 0.76. This implies a shift of 8 mol.-%. With this information it is possible to estimate the critical stress required for fracturing. As the samples consist of non-orientated, crushed grains, it is not possible to analyze the crack spacing.

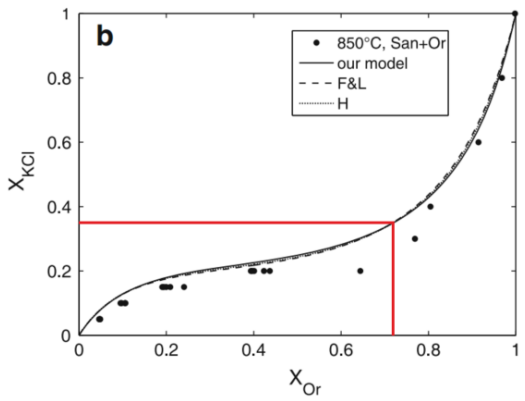


**Figure 17: Na/K fractionation data between salt melt and alkali feldspar for the experiment with $X_{KCl}$ = 0.35; the other compositions are not shown for the sake of clarity; modified after Neusser et al. (2012)**

**Table 2: Results of the experiments conducted in order to determine the critical shift**

| Label | $X_{Or}$ initial | $X_{KCl}$ | $X_{Or}$ exchanged | Shift | Cracks |
|---|---|---|---|---|---|
| SPR7-35-850 | 0.84 | 0.35 | 0.77 | 0.07 | no |
| SPR7-34-850 | 0.84 | 0.34 | 0.76 | 0.08 | yes |
| SPR7-33-850 | 0.84 | 0.33 | 0.75 | 0.09 | yes |
| SPR7-32-850 | 0.84 | 0.32 | 0.74 | 0.10 | yes |
| SPR7-31-850 | 0.84 | 0.31 | 0.73 | 0.11 | yes |

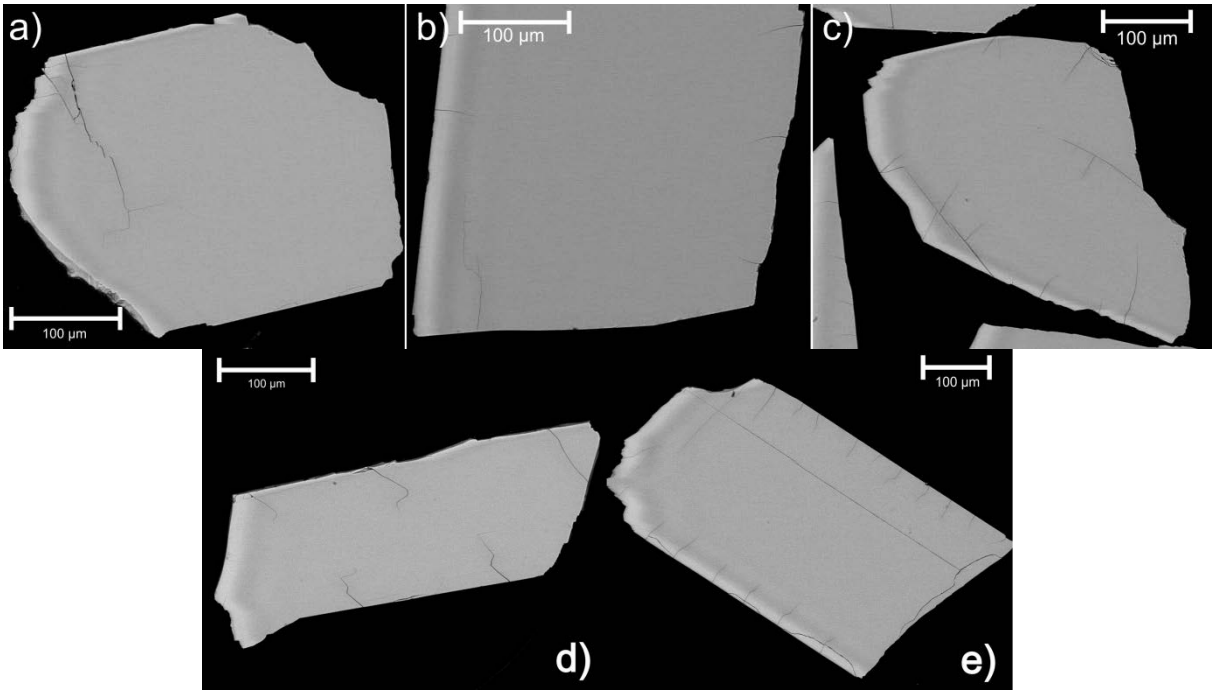


**Figure 18: BSE images of the experiments conducted in order to find the critical shift; for all experiments the starting material was sanidine with $X_{Or}$ = 0.84; the run duration was 7 days; the $X_{KCl}$ of the salt melt was changed systematically**
**a) $X_{KCl}$ = 0.35; $X_{Or}$ exchanged = 0.77 b) $X_{KCl}$ = 0.34; $X_{Or}$ exchanged = 0.76 c) $X_{KCl}$ = 0.33; $X_{Or}$ exchanged = 0.75**
**d) $X_{KCl}$ = 0.32; $X_{Or}$ exchanged = 0.74 e) $X_{KCl}$ = 0.31; $X_{Or}$ exchanged = 0.73**

## 5.3 Dependence of the crack spacing on the chemical shift

For the investigation of the dependence of the crack spacing on the chemical shift sanidine cubes with polished (001) and (010) faces and the initial compositions of $X_{Or}$ = 0.84 and $X_{Or}$ = 0.72 were used. The NaCl/KCl ratio of the salt melt and the run durations were varied. The fractionation diagram between salt melt and feldspar is shown in Figure 19, the compositions for this experiment have been marked. In the sketch depicted in Figure 20, the orientation of the cubes in connection with the orientation of the cracks and further the

orientation of the K- and L-plates are shown. For the investigation of the crack spacing only the samples with run durations of 8 days were used, because of their distinct crack pattern. For run durations of 16 and 32 days, however, the crack pattern was considered to be too complex for further analysis.

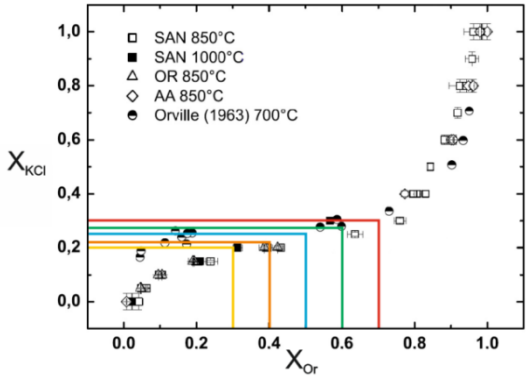


**Figure 19: Na/K fractionation data between salt melt and alkali feldspar for the experiments with defined orientations; modified after Neusser et al. (2012)**

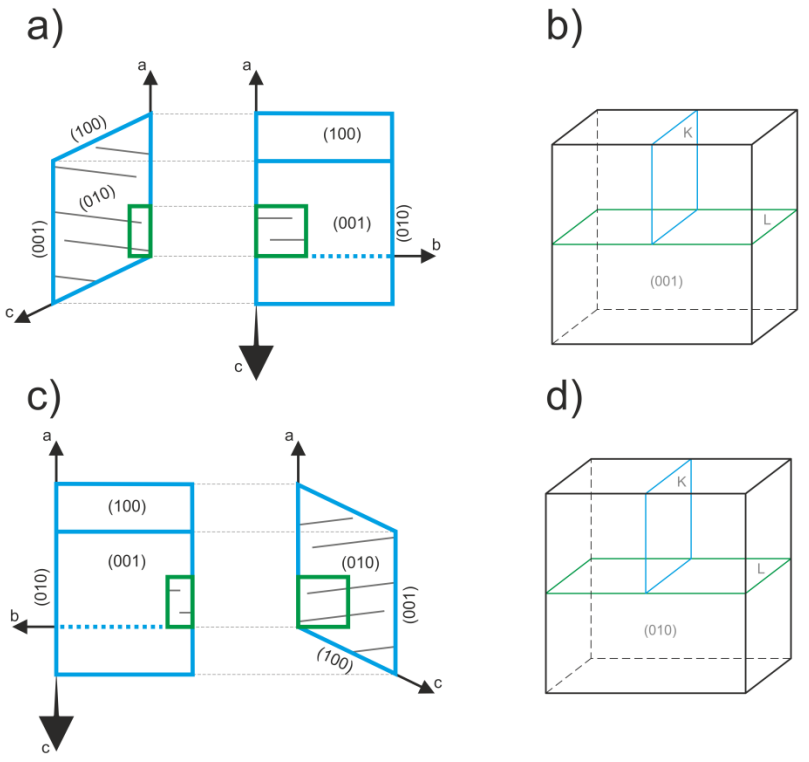


**Figure 20: Orientation of the cubes in connection with the orientation of the cracks**
**a) Cubes with polished (001) faces b) Orientation of the K- and L-plate in the (001) cubes**
**c) Cubes with polished (010) faces d) Orientation of the K- and L-plate in the (010) cubes**

The findings made so far are summarized in Table 3. In Figure 22, Figure 23 and Figure 24 the BSE images of the cut out plates from the cubes are shown.

The crack spacing on the plates of the (001) cubes is partly just apparent crack spacing. This is due to the fact that the plates cut out of the cubes have no distinct orientation but are arbitrarily oriented between the (010) and (100) faces, i.e. are rotated around the c*-axis. Only the polished (001) surfaces are perpendicular to the sample surfaces Thus the cracks do not run exactly perpendicular to the sample surface. Hence, the true spacing still needs to be calculated. This can be obtained by using the following formula (personal communication with R. Abart):

$$h = \frac{sin\varphi}{sin\varphi'} * \frac{tan\varphi'}{tan\varphi} h'$$

with h for the real and h' for the apparent crack spacing, φ for the real angle and φ' for the apparent angle between the positive a-axis and the traces of the cracks.

On the (010) polished faces, however, the real crack spacing can be observed.

The BSE images illustrate that the cracks emanating from the polished surfaces show a very regular spacing which decreases with increasing composition shift. Furthermore the images indicate that the crack spacing for the cracks emanating from the polished (010) surface is narrower than for those emanating from the polished (001) faces. For all samples the observation of the dependence of the crack spacing on chemical shift is confirmed; this leads to the assumption that the samples PR8-20-850, PR8-25-850 and PR8-28-850 were swapped (see Figure 22 and Table 3). Hence, this observation should also apply to this set of samples and the presumably correct order should be PR8-20-850 = $(PR8\text{-}25\text{-}850)_{swapped}$, PR8-25-850 = $(PR8\text{-}28\text{-}850)_{swapped}$ and PR8-28-850 = $(PR8\text{-}23\text{-}850)_{swapped}$.

In Figure 21 the crack spacing is shown as a function of the chemical shift (the samples are taken in the presumably correct order). As the images indicate, the graphs follow an approximately parabolic trend. The samples EPR8-28-850 and EPRb8-28-850, however, go against this trend, since they feature extremely large spacing. This leads to the assumption

that they have not yet reached the regime in which mutual strain of neighboring cracks shields off fracturing and the development of new cracks is therefore prevented. For the samples with $X_{Or}$ = 0.84 as initial composition the crack spacing on the (001) face is larger than on the (010) face. This trend could not be observed for the samples with $X_{Or}$ = 0.72 as initial composition.

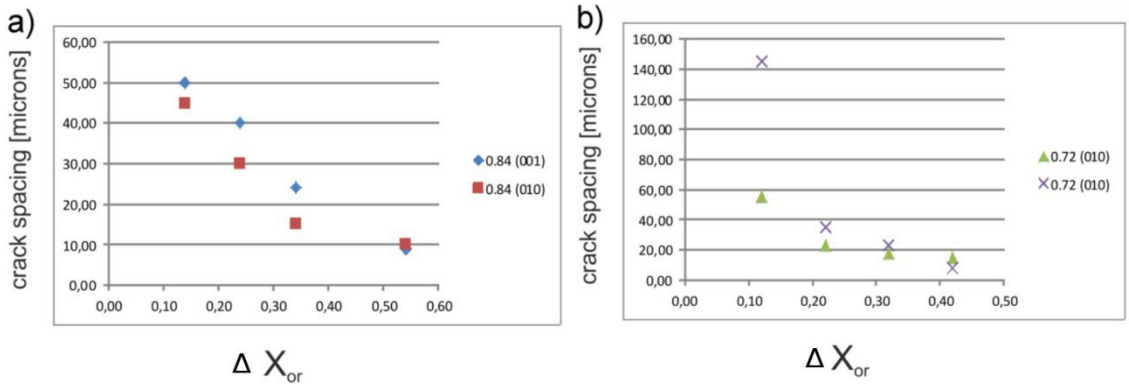


**Figure 21: These diagrams show the crack spacing as a function of the chemical shift**
**a) Sanidine with $X_{Or}$ (initial) = 0.84**
**b) Sanidine with $X_{Or}$ (initial) = 0.72**

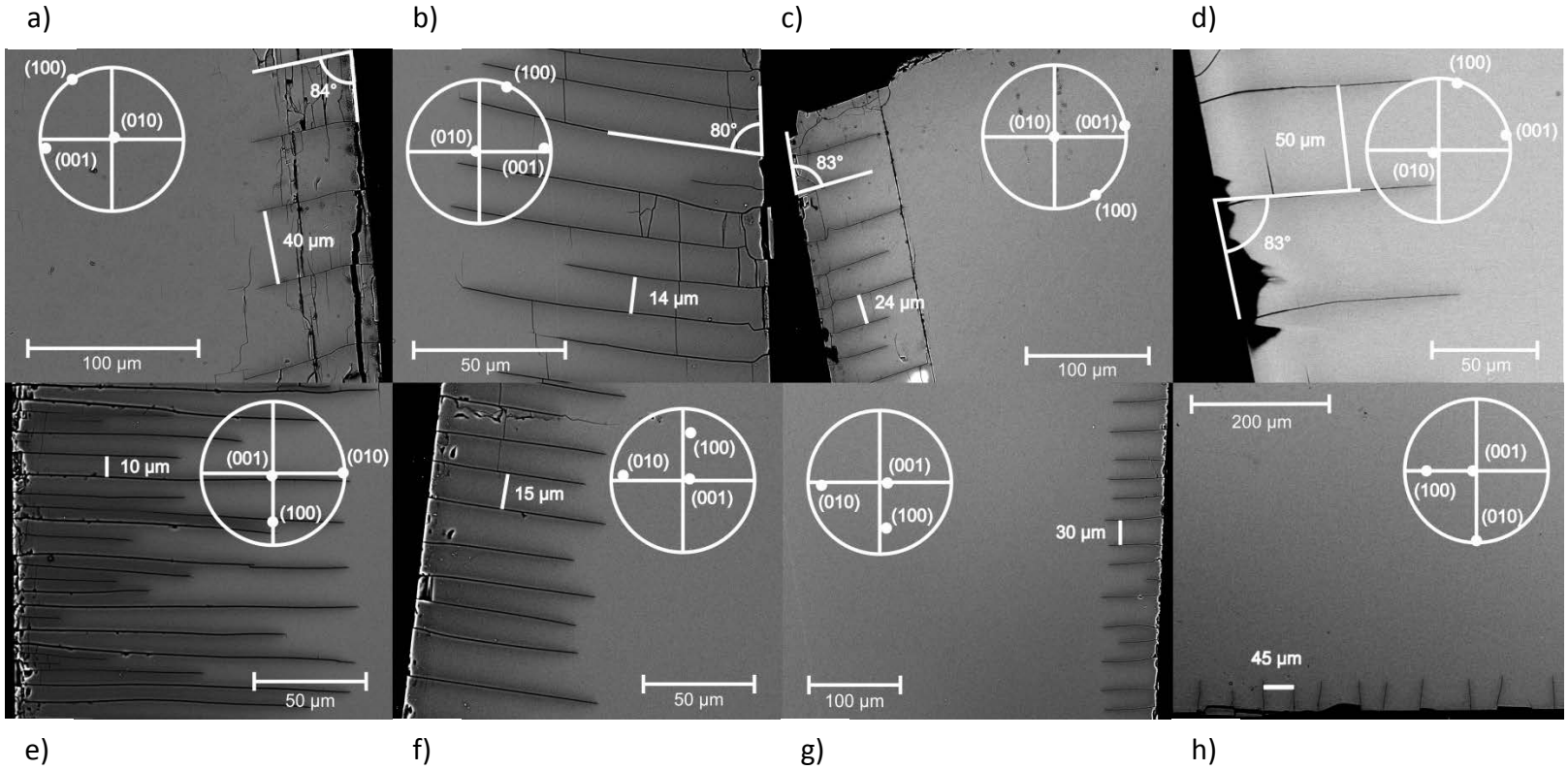


**Figure 22: BSE images of the experiments for the investigation of the dependence of the crack spacing on the chemical shift; initial $X_{Or}$ of the sanidine was 0.84; run duration: 7 days; the $X_{KCl}$ of the salt melt was changed systematically; cubes with (001) and (010) polished faces were used**
**a) $X_{KCl}$ = 0.20; $X_{Or}$ exchanged = 0.30; (001) b) $X_{KCl}$ = 0.25; $X_{Or}$ exchanged = 0.50; (001) c) $X_{KCl}$ = 0.28; $X_{Or}$ exchanged = 0.60; (001) d) $X_{KCl}$ = 0.30; $X_{Or}$ exchanged = 0.70; (001)**
**e) $X_{KCl}$ = 0.20; $X_{Or}$ exchanged = 0.30; (010) f) $X_{KCl}$ = 0.25; $X_{Or}$ exchanged = 0.50; (010) g) $X_{KCl}$ = 0.28; $X_{Or}$ exchanged = 0.60 (010) h) $X_{KCl}$ = 0.30; $X_{Or}$ exchanged = 0.70; (010);**
**d) and h) provided by courtesy of A.-K. Schaeffer**

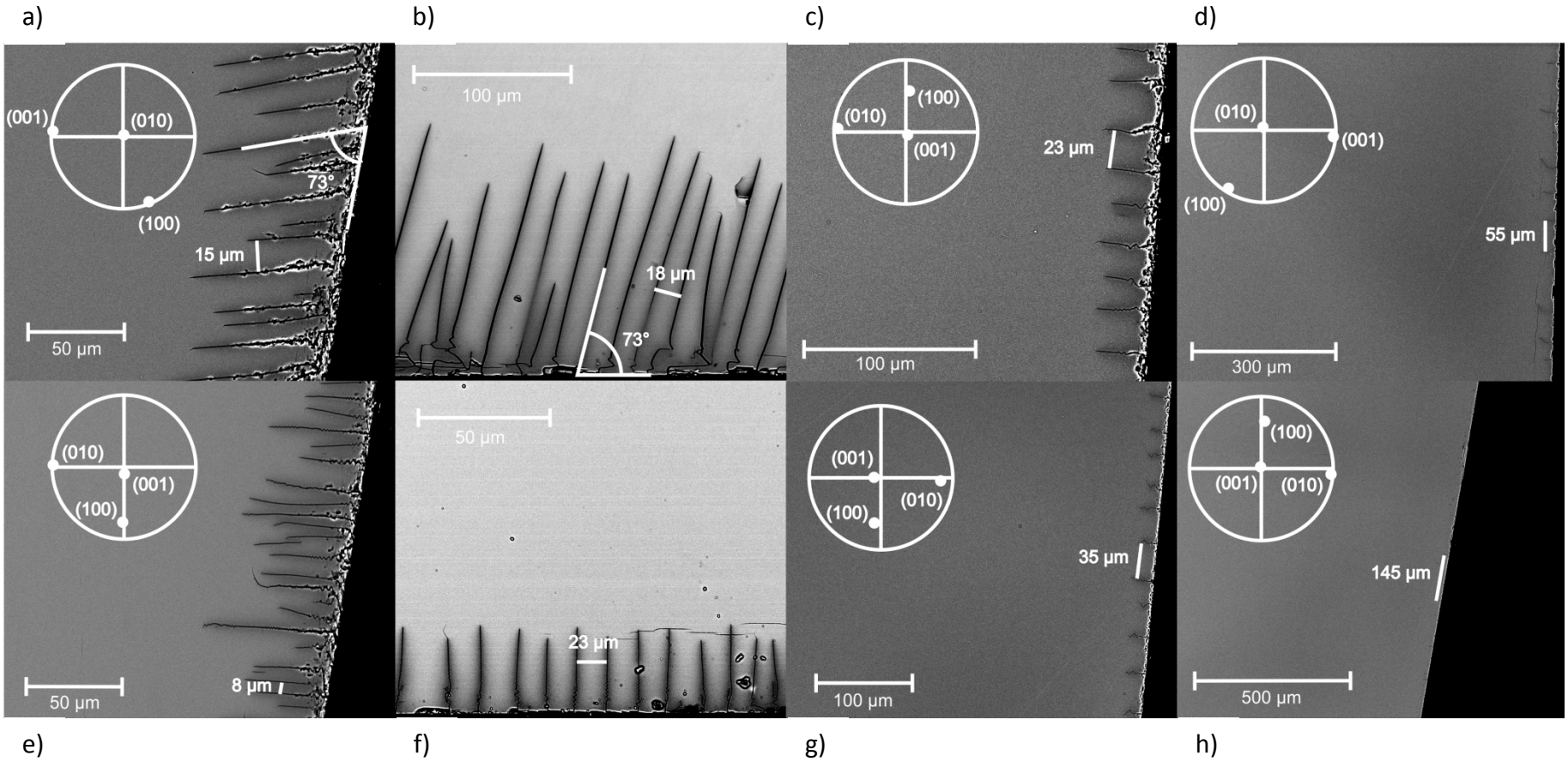


**Figure 23: BSE images of the experiments for the investigation of the dependence of the crack spacing on the chemical shift; initial $X_{Or}$ of the sanidine $X_{Or}$ = 0.72; run duration: 7 days; the $X_{KCl}$ of the salt melt was changed systematically; cubes with (001) and (010) polished faces were used**
**a) $X_{KCl}$ = 0.20; $X_{Or}$ exchanged = 0.30; (001) b) $X_{KCl}$ = 0.22; $X_{Or}$ exchanged = 0.40; (001) c) $X_{KCl}$ = 0.25; $X_{Or}$ exchanged = 0.50 (001) d) $X_{KCl}$ = 0.28; $X_{Or}$ exchanged = 0.60 (001)**
**e) $X_{KCl}$ = 0.20; $X_{Or}$ exchanged = 0.30; (010) f) $X_{KCl}$ = 0.22; $X_{Or}$ exchanged = 0.40; (010) g) $X_{KCl}$ = 0.25; $X_{Or}$ exchanged = 0.50 (010) h) $X_{KCl}$ = 0.28; $X_{Or}$ exchanged = 0.60 (010);**
**b) and f) provided by courtesy of A.-K. Schaeffer**

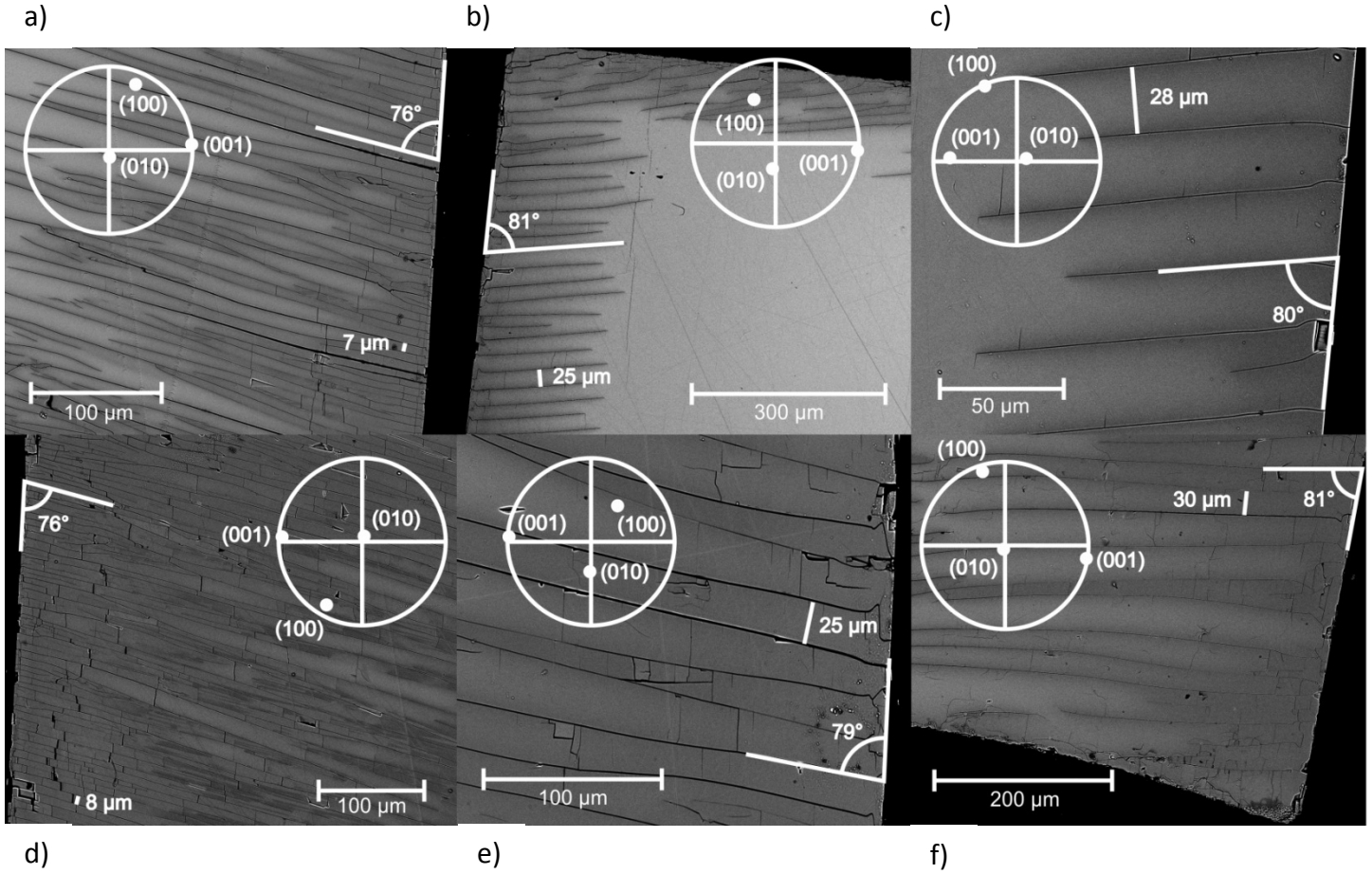


**Figure 24: BSE images of the experiments for the investigation of the dependence of the crack spacing on the chemical shift; initial $X_{Or}$ of the sanidine $X_{Or}$ = 0.84; the $X_{KCl}$ of the salt melt was changed systematically; cubes with (001) were taken; run durations were 16 or 32 days**
**a) $X_{KCl}$ = 0.20; $X_{Or}$ exchanged = 0.30; run durations: 16 days b) $X_{KCl}$ = 0.25; $X_{Or}$ exchanged = 0.50; run durations: 16 days c) $X_{KCl}$ = 0.28; $X_{Or}$ exchanged = 0.60; run durations: 16 days**

**e) $X_{KCl}$ = 0.20; $X_{Or}$ exchanged = 0.30; run durations: 32 days f) $X_{KCl}$ = 0.25; $X_{Or}$ exchanged = 0.50; run durations: 32 days g) $X_{KCl}$ = 0.28; $X_{Or}$ exchanged = 0.60; run durations: 32 days**

**Table 3: Results of the experiments for the investigation of the dependence of the crack spacing on the chemical shift**

| Label | Polished faces | Run durations [d] | $X_{Or}$ initial | $X_{KCl}$ | $X_{Or}$ exchanged | Shift | Apparent crack spacing [µm] | Apparent angle [°] | Real crack spacing [µm] |
|---|---|---|---|---|---|---|---|---|---|
| PR8-20-850 | (001) | 8 | 0.85 | 0.20 | 0.30 | 0.54 | 24 | 83 | 24**** |
| PR8-25-850 | (001) | 8 | 0.84 | 0.25 | 0.50 | 0.34 | 40 | 84 | 40**** |
| PR8-28-850 | (001) | 8 | 0.84 | 0.28 | 0.60 | 0.24 | 14 | 80 | 9**** |
| SP8-30-850* | (001) | 8 | 0.84 | 0.30 | 0.70 | 0.14 | 50 | 83 | 50 |
| PR16-20-850** | (001) | 16 | 0.84 | 0.20 | 0.30 | 0.54 | - | - | - |
| PR16-25-850** | (001) | 16 | 0.84 | 0.25 | 0.50 | 0.34 | - | - | - |
| PR16-28-850** | (001) | 16 | 0.84 | 0.28 | 0.60 | 0.24 | - | - | - |
| PR32-20-850** | (001) | 32 | 0.84 | 0.20 | 0.30 | 0.54 | - | - | - |
| PR32-25-850** | (001) | 32 | 0.84 | 0.25 | 0.50 | 0.34 | - | - | - |
| PR32-28-850** | (001) | 32 | 0.84 | 0.28 | 0.60 | 0.24 | - | - | - |
| PRb8-20-850 | (010) | 8 | 0.84 | 0.20 | 0.30 | 0.54 | -*** | -*** | 10 |
| PRb8-25-850 | (010) | 8 | 0.84 | 0.25 | 0.50 | 0.34 | -*** | -*** | 15 |
| PRb8-28-850 | (010) | 8 | 0.84 | 0.28 | 0.60 | 0.24 | -*** | -*** | 30 |
| SPb-30-850* | (010) | 8 | 0.84 | 0.30 | 0.70 | 0.14 | -*** | -*** | 45 |

| Label | Polished faces | Run durations [d] | $X_{Or}$ initial | $X_{KCl}$ | $X_{Or}$ exchanged | Shift | Apparent crack spacing [µm] | Apparent angle [°] | Real crack spacing [µm] |
|---|---|---|---|---|---|---|---|---|---|
| EP8-22-850* | (001) | 8 | 0.72 | 0.22 | 0.40 | 0.32 | 18 | 73 | 18 |
| EPR8-25-850 | (001) | 8 | 0.72 | 0.25 | 0.50 | 0.22 | 23 | 73 | 23 |
| EPR8-28-850 | (001) | 8 | 0.72 | 0.28 | 0.60 | 0.12 | 55 | 73 | 55 |
| EPRb8-20-850 | (010) | 8 | 0.72 | 0.20 | 0.30 | 0.42 | -*** | -*** | 8 |
| EPb8-22-850* | (010) | 8 | 0.72 | 0.22 | 0.40 | 0.32 | -*** | -*** | 23 |
| EPRb8-25-850 | (010) | 8 | 0.72 | 0.25 | 0.50 | 0.22 | -*** | -*** | 35 |
| EPRb8-28-850 | (010) | 8 | 0.72 | 0.28 | 0.60 | 0.12 | -*** | -*** | 145 |

** Personal communications with A.-K. Schaeffer*

*** These samples with long run durations were not used for the investigation of the crack spacing because of their complex crack pattern.*

**** For the polished (010) faces the crack spacing is real crack spacing.*

***** These samples are presumably swapped; the presumably correct order should be PR8-20-850 = $(PR8\text{-}25\text{-}850)_{swapped}$, PR8-25-850 = $(PR8\ 28\ 850)_{swapped}$ and PR8-28-850 = $(PR8\text{-}20\text{-}850)_{swapped}$. The order given in the table and in the pictures is not changed in the presumably right order but in the real order!*

.

### 5.4 Dependence of the crack orientation on the initial composition of the feldspar

The experiments for the investigation of the dependence of the crack spacing on the chemical shift were done with two sanidines of different initial composition. When interpreting the results it was noticeable that the angle between both the cracks and the a- and c-axis respectively are dependent on the initial composition. For the initial sanidine with $X_{Or}$ = 0.84 the angle between the cracks and the positive a-axis and the positive c-axis is measured as 83-84°; for the other sanidine with $X_{Or}$ = 0.72 as 73° (see Figure 22, Figure 23 and Table 3). In summary it can be stated that with a lower $X_{Or}$ of the initial sanidine the angle between the cracks and the a-axis gets smaller which leads to an increase in the angle between the cracks and the c-axis.

## 6. Discussion

### 6.1 Chemically induced fracturing

The exchange of $K^+$ and $Na^+$ is characterized as a diffusion process. The process only takes place on the cation sublattice while the tetrahedral network remains unmodified; the reaction of the feldspar and the salt melt occurs on the surface and thus an exchanged layer around the grain forms. With the sanidine's shift to more albitic- and more orthoclase-rich compositions, a core-rim structure develops. These exchanged zones on the surface differ from those in the original cores in their $Na^+/K^+$ ratio while the (Al, Si) network still remains intact.

The lattice parameters of the alkali feldspar change with composition. In Figure 25 the composition dependence of the lattice parameters on the mole fraction $X_{Or}$ of the feldspar are summarized according to Kroll and Ribbe (1983). In Table 4 the lattice parameters of sanidine with $X_{Or}$ = 0.84 and analbite with $X_{Or}$ = 0.00 are given. These two phases were chosen for further considerations because they closely represent the composition and (Al, Si) ordering of the samples in this work. The a-, b- and c- lattice parameters shorten from the potassium end member to the sodium end member; the extent, however, varies for the a-, b- and c-axis. The contraction inherent to the shift from a sanidine with $X_{Or}$ = 0.84 to an analbite with $X_{Or}$ = 0.00 amounts to 4.5% in a, to 1.2% in b and to 0.9% in c (see Table 5). The

lattice's shrinkage during the $Na^+/K^+$ exchange and consequently the composition dependent strain is thus extremely anisotropic.

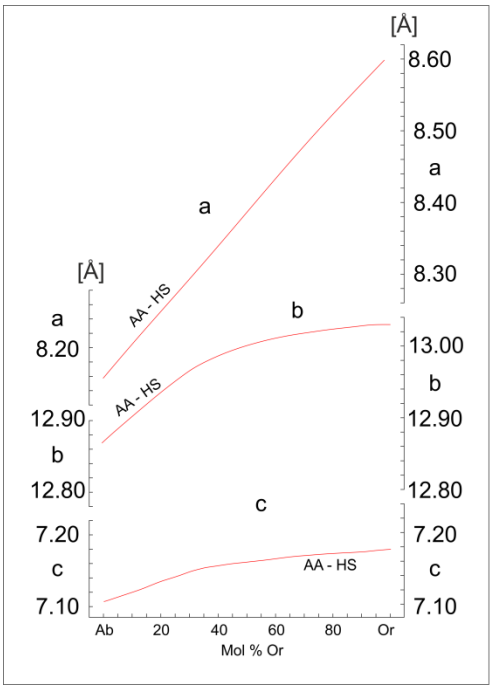


**Figure 25: Dependence of the lattice parameters a, b and c on the mole fraction $X_{Or}$ given for the series analbite - high sanidine; modified after Kroll and Ribbe (1983)**

**Table 4: Lattice parameters for the end members of this work analbite and high sanidine; after Kroll et al. (1986)**

| | **Analbite** | **High Sanidine** |
|---|---|---|
| **An [mol.-%]** | 0.003 | 0.003 |
| **Ab [mol.-%]** | 0.994 | 0.155 |
| **Or [mol.-%]** | 0.003 | 0.842 |
| **a [Å]** | 8.156 | 8.5395 |
| **b [Å]** | 12.871 | 13.0263 |
| **c [Å]** | 7.108 | 7.1713 |
| **α [°]** | 93.483 | 90.000 |
| **β [°]** | 116.448 | 115.987 |
| **γ [°]** | 90.051 | 90.000 |
| **V [$Å^3$]** | 666.4 | 723.4 |

**Table 5: Change of lattice parameters for the shift of a high sanidine to an analbite; data after Kroll et al. (1986)**

| | High Sanidine | Analbite | Change of parameter |
|---|---|---|---|
| **a [Å]** | 8.5395 | 8.156 | 4.5% |
| **b [Å]** | 13.0263 | 12.871 | 1.2% |
| **c [Å]** | 7.1713 | 7.108 | 0.9% |
| **β [°]** | 115.987 | 116.448 | 0.4% |

For this reason fracturing can be detected both with a shift of sanidine to more orthoclase-rich as well as to more albitic compositions. In the shift to albitic compositions, a regular orientated crack pattern in a general crystallographic direction forms. From this, a mechanical analysis of the fracturing is possible. Based on the results of these experiments the critical strain can be determined and hence the critical stress needed for fracturing.

During the exchange with sodium-rich salt melt, a sodium-rich domain develops on the surface of the sanidine grains. This domain forms a misfitting layer on the grain's core which retains its original composition. The volume of the unexchanged core is dominant and thus mechanically much stronger than the rim. To compensate for the chemically induced shrinkage of the lattice in the more sodium-rich surface layer, the lattice itself is elastically strained. Hence the surface layer is under tensile stress. As soon as the strain induced by the chemical shift exceeds a critical value, fracturing occurs.

The estimation of the critical strain and thus the accompanying critical stress for the cracks of first hierarchical level on the (010) face is already given in Neusser et al. (2012). In the following, the critical stress is calculated with new and detailed data derived from this work and a detailed derivation of the stress analysis is given.

### 6.1.1 Determination of the eigenstrain

The eigenstrain tensor represents the stress-free deformation caused by the anisotropic changes of the lattice parameters during the shift of an orthoclase rich to a more sodium rich feldspar. Figure 25 illustrates that the changes in the lattice parameters in connection with variation in the mole fraction $X_{Or}$ are approximately linear in the composition range of interest ($0.00 \leq X_{Or} \leq 0.85$) and therefore the strain could also be seen as linear in this

composition range (Neusser et al. 2012). The calculations for the stress analysis are performed with the lattice parameter data of Kroll et al. (1983) (Table 4). For the calculations two simplifications are made: The (Al, Si) order has to be unchanged and the monoclinic-triclinic transformation at approximately $X_{Or}$ = 0.4 (Kroll et al., 1986) is neglected; the feldspar is treated as being continuously monoclinic. The derivation for the calculation of the eigenstrain is similarly done to Kroll (1984).

The lattice parameters a, b and c describe a position vector **r** for the initial feldspar with $X_{Or}$ = 0.84 and **R** for an exchanged feldspar with $X_{Or}$ = 0.00:

$$\boldsymbol{r} = (x_1, x_2, x_3)$$
$$\boldsymbol{R} = (X_1, X_2, X_3)$$

These two vectors are characterized in a Cartesian reference system. The standard set-up of the reference system with regard to a monoclinic coordinate system is: j parallel to [010], k parallel to [001], and i perpendicular to (100), illustrated in Figure 26.

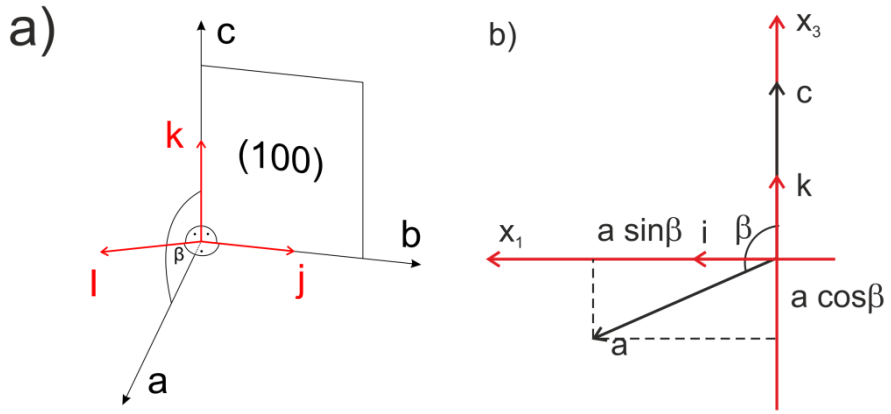


**Figure 26:**
**a) Set up of the Cartesian reference coordinate system i, j and k in reference to a monoclinic coordinate system**
**b) Schematic drawing of the transformation relationships between a, b, c and i, j, k**

The difference vector between the position vector of the initial feldspar **r** and the position vector of the exchanged feldspar **R** is given by the displacement vector **u** (see Figure 27):

$$\boldsymbol{R} = \boldsymbol{r} + \boldsymbol{u}(\boldsymbol{r})$$

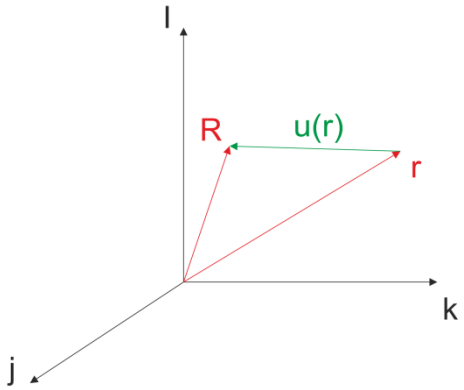


**Figure 27: Schematic drawing of the displacement vector**

The Lagrangian strain tensor is defined as a function of the initial position vector **r** (Nye, 1985):

$$I_{ij} = \frac{\partial u_i}{\partial x_j}$$

$$e_{ij} = \frac{1}{2}\left(I_{ij} + I_{ji}\right)$$

For the simple case of homogeneous deformation the strain is uniform in the entire material and thus $I_{ij}$ = const. as it is appropriate for the lattice contraction during cation exchange of an orthoclase-rich to an albite-rich feldspar. From this it follows:

$$u_i = I_{ij} x_j$$

$$X_i - x_i = I_{ij} x_j$$

$$\begin{pmatrix} X_1 \\ X_2 \\ X_3 \end{pmatrix} = \begin{pmatrix} 1 + I_{11} & I_{12} & I_{13} \\ I_{21} & 1 + I_{22} & I_{23} \\ I_{31} & I_{32} & 1 + I_{33} \end{pmatrix} \begin{pmatrix} x_1 \\ x_2 \\ x_3 \end{pmatrix}$$

or

$$\begin{pmatrix} X_1 \\ X_2 \\ X_3 \end{pmatrix} = M \begin{pmatrix} x_1 \\ x_2 \\ x_3 \end{pmatrix}$$

where M is the matrix of the linear transformation **r** → **R**.

On the basis of the geometrical illustration in Figure 26b the following equations for the relation between the monoclinic and the Cartesian reference system are derived:

$$\boldsymbol{a} = a\,sin\beta\;\boldsymbol{i} + 0\cdot\boldsymbol{j} + a\,cos\beta\;\boldsymbol{k}$$

$$\boldsymbol{b} = 0\cdot\boldsymbol{i} + b\,\boldsymbol{j} + 0\cdot\boldsymbol{k}$$

$$\boldsymbol{c} = 0\cdot\boldsymbol{i} + 0\cdot\boldsymbol{j} + c\,\boldsymbol{k}$$

$$\begin{pmatrix}\boldsymbol{a}\\ \boldsymbol{b}\\ \boldsymbol{c}\end{pmatrix} = \begin{pmatrix} a\,sin\beta & 0 & a\,cos\beta \\ 0 & b & 0 \\ 0 & 0 & c \end{pmatrix}\begin{pmatrix}\boldsymbol{i}\\ \boldsymbol{j}\\ \boldsymbol{k}\end{pmatrix}$$

with the transformation matrix S:

$$S = \begin{pmatrix} a\,sin\beta & 0 & a\,cos\beta \\ 0 & b & 0 \\ 0 & 0 & c \end{pmatrix}$$

Consequential for a vector **r** it is obtained:

$$\boldsymbol{r} = m\boldsymbol{a} + n\boldsymbol{b} + p\boldsymbol{c} = x_1\boldsymbol{i} + x_2\boldsymbol{j} + x_3\boldsymbol{k}$$

$$\boldsymbol{r} = (x_1 \quad x_2 \quad x_3)\begin{pmatrix}\boldsymbol{i}\\ \boldsymbol{j}\\ \boldsymbol{k}\end{pmatrix} = (m \quad n \quad p)\begin{pmatrix}\boldsymbol{a}\\ \boldsymbol{b}\\ \boldsymbol{c}\end{pmatrix} = (m \quad n \quad p)\,S\begin{pmatrix}\boldsymbol{i}\\ \boldsymbol{j}\\ \boldsymbol{k}\end{pmatrix}$$

or $$(x_1 \quad x_2 \quad x_3) = (m \quad n \quad p)S$$

$$\begin{pmatrix}x_1\\ x_2\\ x_3\end{pmatrix} = S^T\begin{pmatrix}m\\ n\\ p\end{pmatrix}$$

The coordinates of the vector **r** are transformed from Cartesian coordinate system into the the monoclinic by:

$$\begin{pmatrix}m\\ n\\ p\end{pmatrix} = \left(S_0{}^{-1}\right)^T\begin{pmatrix}x_1\\ x_2\\ x_3\end{pmatrix}$$

And the coordinates of the vector **R** in the Cartesian coordinate system are given by:

$$\begin{pmatrix} X_1 \\ X_2 \\ X_3 \end{pmatrix} = {S_1}^T \begin{pmatrix} m \\ n \\ p \end{pmatrix} = {S_1}^T \left({S_0}^{-1}\right)^T \begin{pmatrix} x_1 \\ x_2 \\ x_3 \end{pmatrix} = \left({S_0}^{-1} S_1\right)^T \begin{pmatrix} x_1 \\ x_2 \\ x_3 \end{pmatrix}$$

$$\begin{pmatrix} X_1 \\ X_2 \\ X_3 \end{pmatrix} = \begin{pmatrix} 1 + I_{11} & I_{12} & I_{13} \\ I_{21} & 1 + I_{22} & I_{23} \\ I_{31} & I_{32} & 1 + I_{33} \end{pmatrix} \begin{pmatrix} x_1 \\ x_2 \\ x_3 \end{pmatrix} = \left({S_0}^{-1} S_1\right)^T \begin{pmatrix} x_1 \\ x_2 \\ x_3 \end{pmatrix}$$

$$I = \left({S_0}^{-1} S_1\right)^T - id$$

where id is the identity matrix.

Thus the strain tensor is obtained as:

$$e = \frac{\left({S_0}^{-1} S_1\right) + \left({S_0}^{-1} S_1\right)^T}{2} - id$$

The inverse transformation matrix is derived as:

$$S^{-1} = \begin{pmatrix} \frac{1}{a\ sin\beta} & 0 & -\frac{cos\beta}{c\ sin\beta} \\ 0 & \frac{1}{b} & 0 \\ 0 & 0 & \frac{1}{c} \end{pmatrix}$$

Hence the components of the tensile strain are given by:

$$e_{11} = \frac{a_1\ sin\beta_1}{a_0\ sin\beta_0} - 1$$

$$e_{22} = \frac{b}{b_0} - 1$$

$$e_{33} = \frac{c}{c_0} - 1$$

And the components for the shear strain are given by:

$$e_{12} = e_{21} = 0$$

$$e_{13} = e_{31} = \frac{a_1\, cos\beta_1}{2a_0\, sin\beta_0} - \frac{ac_1\, cos\beta_0}{2c_0\, sin\beta_0}$$

$$e_{23} = e_{32} = 0$$

The eigenstrain tensor e for a shift of an orthoclase with $X_{Or}$ = 0.84 to a pure albite is calculated as:

$$e = \begin{pmatrix} -0.0487 & 0 & 0.0050 \\ 0 & -0.0119 & 0 \\ 0.0050 & 0 & -0.0088 \end{pmatrix}$$

The principal strain axes $(e_1)^*$ and $(e_3)^*$ within the (010) plane and the angles between them and the axes i and k are then calculated by (Nye, 1985):

$$(e_1)^* = \frac{1}{2}(e_{11} + e_{33}) - \sqrt{\frac{1}{4}(e_{33} - e_{11})^2 + (e_{13})^2}$$

$$(e_3)^* = \frac{1}{2}(e_{11} + e_{33}) + \sqrt{\frac{1}{4}(e_{33} - e_{11})^2 + (e_{13})^2}$$

$$tan2\theta = \frac{2e_{13}}{e_{33} - e_{11}}$$

$$(e_1)^* = -0.0493$$

$$(e_2)^* = e_{22}$$

$$(e_3)^* = -0.0119$$

$$\theta = 6.9871°$$

To avoid confusion among the components of the principle axes and the components given in the reference coordinate system the components of the principle axes are marked with *.

$(e_1)^*$ and $(e_3)^*$, the directions with the maximum and the minimum contraction, respectively, lie both perpendicular to the b axis and thus within the (010) plane. $(e_3)^*$, the direction with the smallest contraction, forms an angle of Θ = 7.0° with the [001] direction measured from the positive c- to the positive a-axis, depicted in Figure 28.

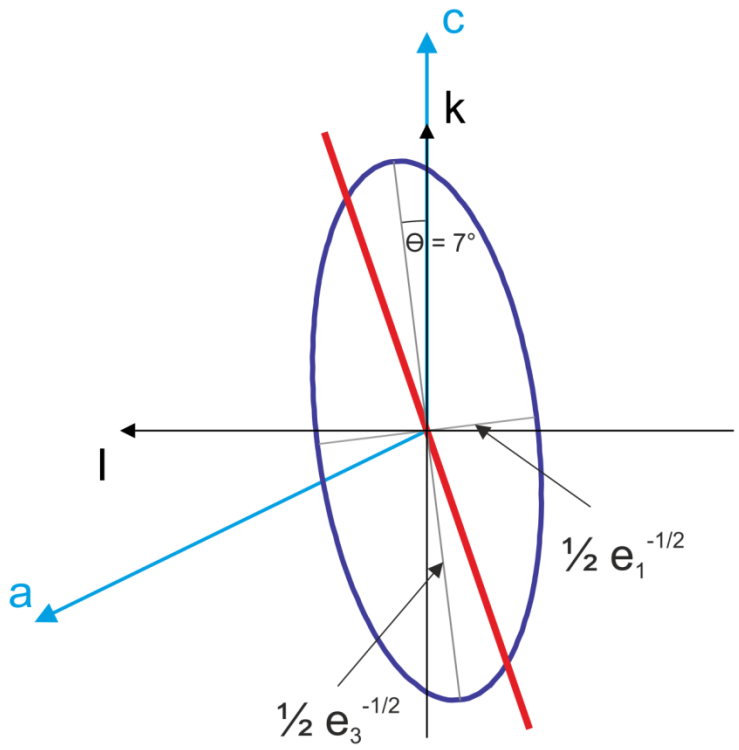


**Figure 28: Projection on (010) showing the principle axes of the eigenstrain tensor e in the coordinate system i, j and k; the red line shows the orientation of the cracks**

The first cracks are detected for an 8 mol.-% shift. The values for the principle axes of the critical strain are than calculated as:

$$\left(e_{1,crit.}\right)^* = -0.0046$$

$$\left(e_{2,crit.}\right)^* = -0.0011$$

$$\left(e_{3,crit.}\right)^* = -0.0008$$

### 6.1.2 Determination of the stress on the (010) plane

The stress analysis is done for an albitic layer developed on the (010) surface.

The relation between stress and strain is given by Hooke's law

$$\sigma_{ij} = C_{ijkl}\, {\epsilon_{kl}}^{el} \ .$$

Introducing the Voigt notation (Nye, 1985):

11 → 1, 22 →2, 33 → 3, 23 and 32 → 4, 13 and 31 → 5, 12 and 21 → 6

this expression is reduced to:

$$\sigma_i = C_{ij}\, {\epsilon_j}^{el}$$

with $C_{ij}$ as the elastic constants. For the following calculations the elastic constants given by Bass (1995) for an albite are used (see Table 6).

**Table 6: Matrix of elastic constants for an albite in [GPa] in Voigt notation by Bass (1995); $C_{ij}$ are given for the standard orientation in monoclinic crystals with j is parallel to [010], k is parallel to [001] and i perpendicular to (100)**

| | $C_{i1}$ | $C_{i2}$ | $C_{i3}$ | $C_{i4}$ | $C_{i5}$ | $C_{i6}$ |
|---|---|---|---|---|---|---|
| $C_{1j}$ | 74 | 36.4 | 39.4 | 0 | -6.6 | 0 |
| $C_{2j}$ | 36.4 | 131 | 31.0 | 0 | -12.8 | 0 |
| $C_{3j}$ | 39.4 | 31.0 | 128 | 0 | -20 | 0 |
| $C_{4j}$ | 0 | 0 | 0 | 17.3 | 0 | -2.5 |
| $C_{5j}$ | -6.6 | -12.8 | -20 | 0 | 29.6 | 0 |
| $C_{6j}$ | 0 | 0 | 0 | -2.5 | 0 | 32 |

To estimate the stress by Hook's law the elastic strain ${\epsilon_j}^{el}$ is required. The total stain $\epsilon_j$ is the sum of the elastic strain ${\epsilon_j}^{el}$ and the eigenstrain $e_j$. Thus the elastic strain ${\epsilon_j}^{el}$ is derived from:

$$\epsilon_j = {\epsilon_j}^{el} + e_j \rightarrow {\epsilon_j}^{el} = \epsilon_j - e_j \ .$$

Considering that the substrate is much stiffer than the thin surface layer the in-plane components of the total strain tensor within the (010) plane are zero (Neusser et al., 2012) (see Figure 29):

$$\epsilon_1 = 0 \rightarrow {\epsilon_1}^{el} = -e_1 = 0.0487$$
$$\epsilon_3 = 0 \rightarrow {\epsilon_3}^{el} = -e_3 = -0.0088$$
$$\epsilon_5 = 0 \rightarrow {\epsilon_5}^{el} = -e_5 = -0.0050.$$

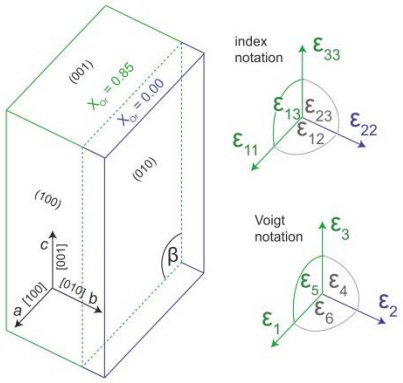


**Figure 29: Components of the strain and the stress tensor with reference to the feldspar unit cell in index notation and Voigt notation; personal communication R. Abart**

The exchange was performed under nearly ambient conditions and thus no pressure was applied on the surface. Hence, the out-of-plane components onto the (010) plane of the stress tensor are zero (Neusser et al., 2012):

$$\sigma_2 = \sigma_4 = \sigma_6 = 0 \ .$$

Inserting this information into Hook's law this yields:

$$\sigma_2 = 0 = -C_{21}e_1 + C_{22}{\epsilon_2}^{el} - C_{23}e_3 - C_{25}e_5$$
$$\sigma_4 = 0 = C_{44}{\epsilon_4}^{el} + C_{46}{\epsilon_6}^{el}$$
$$\sigma_6 = 0 = C_{64}{\epsilon_4}^{el} + C_{66}{\epsilon_6}^{el} \ .$$

And from this it follows:

$${\epsilon_4}^{el} = {\epsilon_6}^{el} = 0$$
$${\epsilon_2}^{el} = \frac{C_{21}e_1 + C_{23}e_3 + C_{25}e_5}{C_{22}}$$
$${\epsilon_2}^{el} = -0.0161.$$

This is consistent with the effect of the monoclinic symmetry of the feldspar on a second rank tensor; hence, the shear components ${\epsilon_4}^{el}$ and ${\epsilon_6}^{el}$ have to be zero.

Therefore all components for the elastic strain tensor ${\epsilon_j}^{el}$ are given:

$$\epsilon^{el} = \begin{pmatrix} 0.0487 \\ -0.0161 \\ 0.0088 \\ 0 \\ -0.0050 \\ 0 \end{pmatrix}.$$

The stress tensor for a shift of an orthoclase with $X_{Or}$ = 0.84 to a pure albite can now be calculated, based on Hooke's law:

$$\sigma = \begin{pmatrix} 3.3972 \\ 0 \\ 2.6481 \\ 0 \\ -0.4386 \\ 0 \end{pmatrix}.$$

Finally, the equations for the principle stress values and directions are the same as those for the principle strains (Nye, 1985):

$$(\sigma_1)^* = \frac{1}{2}(\sigma_{11} + \sigma_{33}) - \sqrt{\frac{1}{4}(\sigma_{33} - \sigma_{11})^2 + (\sigma_{13})^2}$$

$$(\sigma_2)^* = \sigma_{22}$$

$$(\sigma_3)^* = \frac{1}{2}(\sigma_{11} + \sigma_{33}) + \sqrt{\frac{1}{4}(\sigma_{33} - \sigma_{11})^2 + (\sigma_{13})^2}$$

$$tan2\varphi = \frac{2\sigma_{13}}{\sigma_{33} - \sigma_{11}}$$

$$(\sigma_1)^* = 2.4459\ GPa$$

$$(\sigma_2)^* = 0$$

$$(\sigma_3)^* = 3.5994\ GPa$$

$$\varphi = 24.7514°$$

$(\sigma_3)^*$, the direction with the maximum value forms an angle of φ = 24.8° with the [001] direction measured from the positive c- to the positive a-axis. $(\sigma_1)^*$, illustrated in Figure 30. The dominant set of cracks is orientated perpendicular to $(\sigma_3)^*$, which corresponds to the direction of maximum tensile stress necessary for brittle fracturing. The exsolution lamellae of cryptoperthitic feldspars extend in $(\bar{6}01)$ or $(\bar{8}01)$ faces (Bollmann and Nissen, 1968) which coincides with the planes of the cracks, shown in Figure 31. They are orientated in a manner to minimize the coherence strain energy.

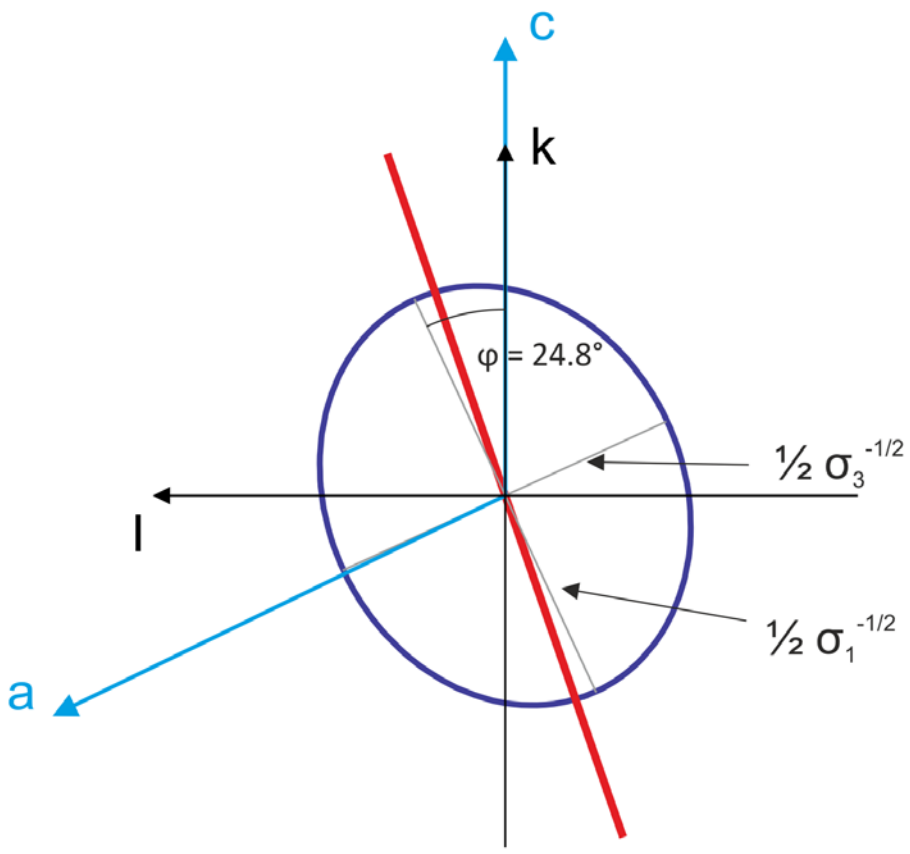


**Figure 30: Projection on (010) showing the principle axes of the stress tensor σ in the coordinate system i, j and k; the red line shows the orientation of the cracks**

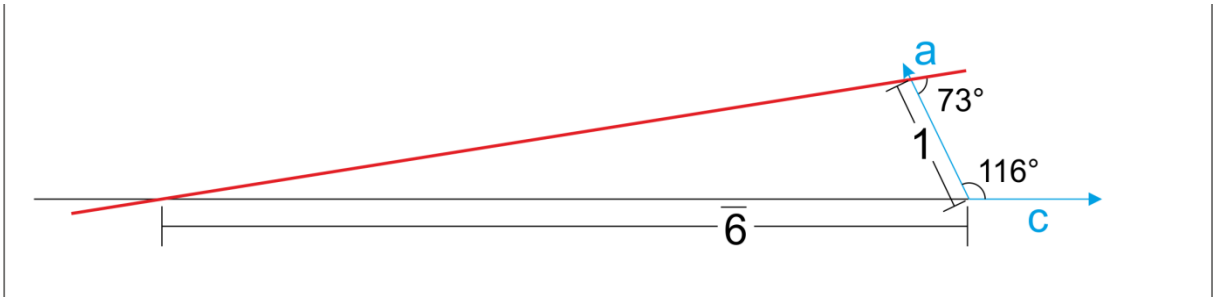


**Figure 31: Schematic drawing of the ($\bar{6}01$) orientation of the exsolution lamellae**

The above mentioned stress values correspond with a composition change of a sanidine end member to an analbite. In this work fracturing occurs at a shift of 8 mol.-%. Thus that yields for the principle axes of the critical stress:

$$\left(\sigma_{1,crit.}\right)^{*} = 0.2329\ GPa$$
$$\left(\sigma_{3,crit.}\right)^{*} = 0.3428\ GPa$$

## 6.2 Fracture mechanics

Fracture mechanics deals with the description of crack propagation under stress. The parameter which describes the stress condition responsible for crack propagation is the stress intensity factor K which has the unit $\mathrm{MPa}\sqrt{\mathrm{mm}}$.

According to the movement of the crack planes, three different crack modes of crack opening can be distinguished, see Blumenauer and Pusch (1993):

- Mode I: The crack opening is perpendicular to the crack surface. Thus the sample is under tensile stress
- Mode II: The crack surfaces are moved parallel against each other and perpendicular to the crack propagation. The sample is under shear stress.
- Mode III: The crack surfaces are moved parallel against each other and transversely to the direction of crack propagation. The sample is under torsion stress.

The cracks developing due to composition shift in the exchanged alkali feldspars are mode I cracks. In Tada et al. (1985) K is defined for mode I on the condition that fracturing occurs in a regime where it is subject to stress shielding by neighboring cracks as:

$$K_I = \sigma\sqrt{a}$$

Hence, it is possible to formulate a criterion for fracturing (Heckel, 1991):

$$K_I \geq K_{Ic}$$

This describes the onset of the propagation of a crack by reaching the critical value, denoted as the fracture toughness or critical stress intensity factor, $K_{Ic}$ (Blumenauer and Pusch, 1993). The fracture toughness is the key material parameter to describe the material behaviour during brittle fracturing.

The fracture toughness $K_{Ic}$ for alkali feldspar is calculated on the basis of the sample with run durations of 8 days and a 24 mol.-% composition shift (PRb-28-850). The crack length $a$ is 60 µm and the crack spacing $2h$ is 30 µm. The crack spacing factor s is defined as (Tada et al. 1985):

$$s = \frac{a}{a+h} = 0.8$$

In this regime fracturing is subject to stress shielding by neighboring cracks.

When inserting $\sigma$ = 1.03 GPa for the tensile stress $K_{Ic}$ is obtained as:

$$K_I = \sigma\sqrt{h} = 400\ MPa\sqrt{mm}$$

The value for $K_{Ic}$ of alkali feldspar is within the range of glass and ceramics (Blumenauer and Pusch, 1993).

## 7. Conclusion

During the exchange of alkali feldspar with NaCl – KCl salt melt only the cations diffuse while the (Al, Si) network remains unchanged. This effect is comparable to exsolved cryptoperthites. They develop strained potassium- and sodium- rich domains and thus exhibit typical microstructures. When sanidine is shifted to albitic-rich compositions a hierarchical crack pattern forms. The first order cracks have a general crystallographic (h0l) plane whereas the cracks of the second hierarchical level run parallel to the first order and follow the (001) cleavage plane. The crack formation during the exchange of sanidine with sodium-rich salt melt is due to the composition dependent, anisotropic contraction of the lattice parameters. During this process a misfitting albite-rich layer forms on a core featuring the original orthoclase-rich composition. To induce fracturing a critical stress value has to be exceeded; before this critical stress is reached, the lattice of the albitic rim only displays elastic stretching. In this work fracturing was detected at an 8 mol.-% shift of the sanidine to a more sodium-rich composition, corresponding to a critical stress of 343 MPa. Cracks of the first hierarchical level are orientated perpendicular to the direction of the maximum tensile stress, i.e. perpendicular to $\sigma_1$. $\sigma_1$ does, however, not coincide with the direction of the maximum shrinkage. The cracks of the first hierarchical level show the same orientation as the lamellae of perthitic feldspar. These exsolution lamellae are also arranged perpendicular to the direction of the highest tensile stress to minimize the coherence strain energy. The crack spacing decreases with increasing composition shift. This is due to the fact that the tensile strain increases with the composition-dependent, anisotropic contraction of the lattice parameters associated with decreasing shift. The cracks of the first hierarchical level are then penetrated by the ambient salt melt resulting in new misfitting surfaces prone to further fractioning perpendicular to the maximum tensile stress within these planes. The stress analysis within the (h0l) and (001) planes showed that these cracks extend perpendicular to $\sigma_2$, the component with the highest of the stress tensor within these planes. For the Volkesfeld sanidines with $X_{Or}$ = 0.84 the crack spacing is larger on the (001) than on the (010) polished face. This can be explained with the fact that on (010) the stress component $\sigma_1$ is higher. The angle between the positive a-axis and the plane of the cracks varies as a function of the initial composition of the feldspar. It is assumed that the elastic

constants for the feldspars are also dependent on the composition of the feldspar. Unfortunately, there are no publications to confirm this hypothesis. The very regular spacing of the cracks emanating from the polished surface indicates stress shielding between the neighboring cracks. Thus a fracture toughness of $400\ \mathrm{MPa}\sqrt{\mathrm{mm}}$ can be derived, comparable with values for glass and ceramics.

## 8. Literature


Abart, R.; Pertishcheva, E.; Wirth, R. and Rhede, D. (2009). Exsolution by spinodal decomposition II: Perthite formation during slow cooling of anatexites from Ngoronghoro, Tanzania. American Journal of Science, 309, 450-475.

Bass, J. D. (1995). Elasticity of Minerals, Glasses, and Melts. AGU Reference Shelf 2, 45-63.

Blumenauer, H. and Pusch, G. (1993). Technische Bruchmechanik (3 ed.). Deutscher Verlag fuer Grundstoffindustrie: Leipzig.

Bollmann, W. and Nissen, H.-U. (1968). A Study of Optimal Phase Boundaries: The Case of Exsolved Alkali Feldspars. Acta Crystallographica, 24, 546-557.

Brown, W. L.; Becker, S. M. and Parsons, I. (1983). Cryptoperthites and Cooling Rate in a Layered Syenite Pluton: A Chemical and TEM Study. Contributions to Mineralogy and Petrology, 82, 13-25.

Brown, W. L. and Parsons, I. (1984). Exsolution and coarsening mechanisms and kinetics in an ordered cryptoperthite series. Contributions to Mineralogy and Petrology, 86, 3-18.

Christoffersen, R.; Yund, R. A. and Tullis, J. (1983). Inter-diffusion of K and Na in alkali feldspars: diffusion couple experiments. American Mineralogist, 68, 1126-1133.

Crank, J. (1975). The Mathematics of Diffusion (2 ed.). Clarendon Press: Oxford.

Deer, W. A. and R. A. Howie, J. Z. (2001). Rock-Forming Minerals (2 ed., Vol. 4A). The Geological Society: London.

Demtroeder, K. (2011). Untersuchung zur Al/Si-Ordnung an Sanidin-Megakristallen aus der Eifel. Masterarbeit, Ruhr-Universität Bochum.

Flude, S.; Lee, M. R.; Sherlock, S. C.; and Kelley, S. P. (2012). Cryptic microtextures and geological histories of K-rich alkali feldspars revealed by charge contrast imaging. Contributions to Mineralogy and Petrology, 163, 983-994.

Heckel, K. (1991). Einfuehrung in die technische Anwendungen der Bruchmechanik (3 ed.). Hansa: Muenchen, Wien.

Huston, E. L.; Chan, J. W.; and Hilliard, J. E. (1966). Spinodal decomposition during continuous cooling. Acta Metallurgica, 14, 1053-1062.

Kroll, H. (1984). Thermal expansion of alkali feldpars. In Brown, W. L., Feldspars and Feldspathoids. Springer Verlag: New York.

Kroll, H. and Ribbe, P. H. (1983). Lattice parameters, composition and Al,Si order in alkali feldspars. In Ribbe, P. H., Feldspar Mineralogy (Vol. 2, 57-100). Reviews in Mineralogy.

Kroll, H.; Schmiemann, I., and Coelln, G. v. (1986). Feldspar solid solutions. American Mineralogist, 71, 1-16.

Neusser, G.; Abart, R.; Fischer, F. D.; Harlov, D. and Norberg, N. (2012). Experimental Na/K exchange between alkali feldspar and an NaCl–KCl salt melt: chemically induced fracturing and element partitioning. Contributions to Mineralogy and Petrology

Norberg, N.; Neusser, G.; Wirth, R. and Harlov, D. (2011). Microstructural evolution during experimental albitization of K-rich alkali feldspar. Contributions to Mineralogy and Petrology., 162, 531-546.

Nye, J. F. (1985). Physical properties of crystals. Oxford University: New York.

Okrusch, M. and Matthes, S. (2009). Mineralogie: Eine Einfuehrung in die spezielle Mineralogie, Petrologie und Lagerstaettenkude (8 ed.). Springer Verlag: Berlin, Heidelberg, New York.

Orville P. M. (1963). Alkali ion exchange between vapor and feldspar phases. American Journal of Science, 261, 201-237.

Parsons, I.; Gerald, J. D.; Ivanic, J. K. and Golla-Schindler, U. (2010). Time–temperature evolution of microtextures and containedfluids in a plutonic alkali feldspar during heating. Contribution of Mineral Petrology, 160, 155-180.

Phillips, M. W. and Ribbe, P. H. (1973). The structures of monoclinic potassium rich feldspars. American Mineralogist, 58, 263-270.

Pluemper, O. and Putnis, A. (2009). The complex Hydrothermal history of granitic rocks: Multiple feldspar replacement reactions under subsolidus coditions. Journal of Petrology, 50, 967-987.

Putnis, A. (2009). Mineral replacement reactions: from macroscopic observations to microscopic mechanisms. Mineralogic magazine, 66, 689-708.

Ribbe, P. H. (1986). Chemistry, Structure and Nomenclature of Feldspars. In Ribbe, P. H., Feldspar Mineralogy (2 ed., Vol. 2, 1-19). Mineral Society of America.

Sipling, P. J. and Yund, R. A. (1976). Experimental determination of the coherent solvus for sanidine-high albite. American Mineralogist, 61, 897-906.

Tada, H., Paris, P. C. and Irwin, G. R. (1985). The stress analysis of cracks handbook (2 ed.). Paris Productions: St. Louis, MO.

Yuguchi, T. and Nishiyama, T. (2007). Cooling process of a granitic body deduced from the extents of exsolution and deuteric sub-solidus reactions: Case study of the Okueyama granitic body, Kyushu, Japan. Elsevier, 97, 395-421.

Yund, R. A. and Davidson, P. (1978). Kinetics of lamellar coarsening in cryptoperthites. American Mineralogist, 63, 470-477.

## 9. Acknowledgement

Zuerst möchte ich mich bei Herrn Prof. Abart bedanken für dieses interessante Thema und die Betreuung dieser Arbeit. Er hat es mir durch mehrere Posterpräsentationen auf Tagungen ermöglicht, meine ersten Erfahrungen im wissenschaftlichen Arbeiten zu machen, wofür ich sehr dankbar bin. Des Weiteren habe ich sehr viel Vertrauen und Freiheit bekommen, er war aber auch jeder Zeit bereit für Diskussionen.

Weiter geht natürlich ein großes Dankeschön an Anne für die tolle Begleitung dieser Arbeit. Sie war immer da für Fragen und Diskussionen und immer bereit mir bei Problemen zu helfen.

Vielen Dank auch an Frau Dr. E. Petrishcheva für die Unterstützung bei der Stress-Analyse. Sie hatte jeder Zeit ein offenes Ohr für mich. Unsere Diskussionen waren mir sehr hilfreich und ich habe viel dabei gelernt.

Ein besonderer Dank geht an Frau Dr. G. Habler die mit mir an der Quanta BSE Bilder und EBSD pattern aufgenommen hat, sie betreute mich an der Elektronenstrahlmikrosonde und erklärte mir die Technik.

Für die Einweisung und Hilfestellungen am InspectS möchte ich Hugh danken.

Zuletzt geht selbstverständlich noch ein großes Danke an David, Edith und Sophi, die mich während meiner ganzen Studienzeit, aber im Besonderen in den letzten Wochen beim Schreiben dieser Arbeit immer wieder motiviert haben.

## 10. Appendix

# Abstract - English

Several millimeter sized cubes of gem-quality alkali feldspars with a mole fraction of $X_{Or}$ = 0.84 and $X_{Or}$ = 0.72 and with polished (010) or (001) surfaces were reacted with a NaCl – KCl salt melt. Thees experiments were performed in quartz glass tubes at close to ambient pressure and temperatures of 850 °C at a time period of 8 days. The $X_{KCl}$ of the salt melt was varied on the basis of the Na/K fractionation data for feldspar – salt equilibria in order to shift the feldspar to more sodium-rich compositions. The exchange between the salt melt and the feldspar occurred during the $Na^+/K^+$ interdiffusion while the (Al, Si) tetrahedral framework remained intact.

When a critical composition shift is exceeded, a hierarchical system of cracks forms due to the composition dependence of the feldspar's lattice parameters. The most noticeable set of subparallel cracks extends in a (h0l) plane, enclosing an angle of about 83° for sanidine with initial composition $X_{Or}$ = 0.84 and 73° for sanidine with initial composition $X_{Or}$ = 0.72 with the [100] direction (measured from positive [100] to positive [001]). Locally, a second set of cracks forms, which follows the (010) cleavage planes.

The crack pattern reflects the strong anisotropy of the chemically induced change in lattice parameters; shortening in the [100] direction exceeds that in the [010] and the [001] directions by a factor of five for a composition change of a potassium to a sodium feldspar. During the cation exchange an albite-rich misfitting surface layer develops onto the sanidine grain. In due to the stiffer substrate the surface layer is elastically strained until a critical value is reached and fracturing occurs. Crack formation is detected at a shift of 8 mol.-%; therefore a critical stress of 343 MPa can be calculated.

The first hierarchical level cracks are orientated perpendicular to the maximum tensile stress as it is expected for brittle fracturing. This is the same direction as it is observed for the perthitic exsolution lamellae which are orientated in a manner to minimize the coherence strain energy. These cracks are penetrated by the salt melt and form a new surface for

cation diffusion. Hence, a new misfitting surface layer is formed and the second order cracks form perpendicular to the direction of maximum tensile stress within the (h0l) plane.

The first order cracks emanating from the polished surfaces show very regular spacing. The crack spacing decreases with increasing composition shift. Due to this fact the fracture toughness $K_{Ic}$ for alkali feldspar is estimated about 400 $\mathrm{MPa}\sqrt{\mathrm{mm}}$.

## Abstract - Deutsch

Millimeter große Alkalifeldspatwürfel mit polierten (010) und (001) Flächen wurden mit NaCl– KCl-Salzschmelze ausgetauscht. Die Ausgangszusammensetzungen der Sanidine mit Edelsteinqualität betrugen $X_{Or}$ = 0.84 und $X_{Or}$ = 0.72. Die Experimente wurden in Quarzglasröhrchen unter Atmosphärendruck bei 850 °C mit einer Laufzeit von 8 Tagen durchgeführt. $X_{KC}$ der Salzschmelze wurde auf Grundlage des Austauschdiagramms von Alkalifeldspat und NaCl – KCl so gewählt, dass Sanidin zu Albit-reicheren Zusammensetzungen verschoben wurde. Der Austausch des Feldspates mit der Salzschmelze findet durch Interdiffusion der Kationen statt, während das Tetraeder-Gitter nicht verändert wird.

Ab einem kritischen Ausmaß der Zusammensetzungänderung bildet sich ein hierarchisches Rissmuster aufgrund der Zusammensetzungsabhängigkeit der Gitterparameter. Das deutlich ausgebildete Set an parallelen Rissen verläuft entlang (h0l) und schließt einen Winkel von 83° für einen Sanidin mit der Ausgangszusammensetzung $X_{Or}$ = 0.84 und einen Winkel von 73° für einen Sanidin mit der Ausgangszusammensetzung $X_{Or}$ = 0.72 mit der [001] Richtung ein (gemessen von der positiven [001] Richtung zur positiven [010] Richtung). Lokal bildet sich ein zweites Set an Rissen, das entlang der (010) Spaltebenen verläuft.

Das Rissmuster wird aufgrund der starken Anisotropie der Gitterparameter der Alkalifeldspate erzeugt. Bei der Zusammensetzungänderung von einem Kalium-Feldspat zu einem Natrium-Feldspat verkürzt sich die [001] Richtung 5-mal stärker als die [010] und die [001] Richtung. Durch Kationenaustausch bildet sich um das Sanidin-Korn ein Albit-reicher Saum. Da die beiden Gitter sich in der Größe unterscheiden wird der Saum, der den größeren und damit steiferen Kern umgibt, elastisch gedehnt. Sobald jedoch ein kritischer Wert in der Dehnung überschritten ist, bilden sich Risse. Die ersten Risse wurden bei einer Zusammensetzungänderung von 8 Mol.-% festgestellt, woraus sich eine Spannung von 343 MPa berechnen lässt.

Die Risse der ersten hierarchischen Ordnung sind senkrecht zur Richtung der maximalen Zugspannung orientiert, was für die Bildung von spröden Rissen zu erwarten ist. Die Risse

haben dieselbe Orientierung wie die Entmischungslamellen von Alkalifeldspäten, die so orientiert sind, dass sie die Spannungsenergie, die durch das kohärente Gitter aufgebaut wird, minimieren. In die Risse der ersten Ordnung kann die Salzschmelze eindringen. Dadurch wird auf den Rissflächen eine neue Oberfläche parallel zu (h0l) für Kationenaustausch geschaffen. Auf diesen bildet sich erneut eine nicht passende Oberfläche in der sich senkrecht zur maximalen Zugspannung Risse bilden.

Die Risse der ersten Ordnung, die von den polierten Oberflächen aus losgehen, zeigen regelmassige Rissabstände, die mit zunehmender Zusammensetzungänderung enger werden. Aufgrund dieser Tatsache lässt sich eine Bruchzähigkeit von 400 $\mathrm{MPa}\sqrt{\mathrm{mm}}$ für Alkalifeldspate bestimmen.

# Lebenslauf

## Persönliche Angaben

| | |
|---|---|
| Name | Katharina Sarah Scheidl |
| Geburtsdatum | 08.06.1985 in München |
| Familienstand | ledig |
| Staatsangehörigkeit | deutsch |

## Schulbildung

| | |
|---|---|
| Gymnasium bis Abitur<br>Abschluss August 2005 | Dante-Gymnasium, München |

## Freiwilliges Soziales Jahr

| | |
|---|---|
| Sept. 2005 – Aug. 2006 | Heilpädagogische Tagesstätte der<br>Lebenshilfe München Kinder und Jugend GmbH |

## Studium

| | |
|---|---|
| Okt. 2006 – Okt. 2007 | Bachelor Physik, LMU München |
| Okt. 2007 – Aug. 2010 | Bachelor Geowissenschaften, Vertiefungsrichtung Mineralogie<br>TU / LMU München<br>Thema der Bachelorarbeit: Epitaktisches Wachstum eines Approximanten auf quasikristallinem Substrat<br>(Betreuer Prof. Gille) |
| seit Oktober 2010 | Master Erdwissenschaften, Vertiefungsrichtung Mineralogie und Kristallographie Universität Wien<br>Thema der Masterarbeit: Coherence strain effects in alkali feldspar<br>(Betreuer Prof. Abart) |

## Berufliche Erfahrungen

| | |
|---|---|
| Sept. 2008 | studentische Aushilfe SGS, Bereich Consumer Testing Services / CQE: Labortätigkeiten im Bereich der Umweltbeprobung |
| Feb. – April 2010 | Praktikum Knauf Gips KG, Rohstoffsicherung: geologische Kartierung |
| seit Mai 2011 | studentische Hilfskraft Geologische Bundesanstalt, Rohstoffgeologie: quantitative Analyse von Tonmineralen anhand Pulverdiffraktometrie |